

Agentic Exploration of Physics Models

Maximilian Nägele* and Florian Marquardt

*Max Planck Institute for the Science of Light, Staudtstraße 2, 91058 Erlangen, Germany and
Department of Physics, Friedrich-Alexander Universität Erlangen-Nürnberg, Staudtstraße 5, 91058 Erlangen, Germany*

The process of scientific discovery relies on an interplay of observations, analysis, and hypothesis generation. Machine learning is increasingly being adopted to address individual aspects of this process. However, it remains an open challenge to fully automate the heuristic, iterative loop required to discover the laws of an unknown system by exploring it through experiments and analysis, without tailoring the approach to the specifics of a given task. Here, we introduce SciExplorer, an agent that leverages large language model tool-use capabilities to enable exploration of systems without any domain-specific blueprints, and apply it to physical systems that are initially unknown to the agent. We test SciExplorer on a broad set of models spanning mechanical dynamical systems, wave evolution, and quantum many-body physics. Despite using a minimal set of tools, primarily based on code execution, we observe impressive performance on tasks such as recovering equations of motion from observed dynamics and inferring Hamiltonians from expectation values. The demonstrated effectiveness of this setup opens the door towards similar scientific exploration in other domains, without the need for finetuning or task-specific instructions.

In recent years, specialized machine learning techniques have been increasingly employed to address various individual aspects of the scientific discovery process, for example, by suggesting new experiments [1–3], predicting or analyzing experimental results [4–6], learning meaningful representations of data [7, 8], or recovering governing equations as symbolic expressions [9]. However, these tools are typically designed to solve a specific task in a specific setting. Large-language models (LLMs) exceed the capabilities of the usual machine learning approaches in several ways: Famously, they can work on a large variety of tasks without any specialized training data set, often in a zero-shot manner, i.e. without even providing a few exemplary solution templates [10]. They work well with arbitrarily structured input, including multimodal data mixing text and images [11] and can reason, producing a textual record of their arguments. As a result, LLMs can work well in situations where heuristic approaches and some level of creativity are required, all the time relying on their general factual knowledge garnered during training. For the tasks we will consider here, this includes in particular math and physics knowledge, supplemented by outstanding abilities in coding [12, 13]. At the same time, the greatest weakness of LLMs is their propensity to hallucinate. One approach to overcome this to some extent, also relied on in the present work, is to focus on scenarios where some level of self-correction is possible, with independent ways to check and repudiate results [14].

In the past few years, the power of LLMs has been boosted by agentic behavior (tool use). By allowing the LLM to call up external software tools, one can combine the reliability of those tools with the heuristics and general knowledge of the LLM [15]. First examples of agentic behavior have recently been introduced into several sci-

entific domains. In computer science, LLMs conduct complex coding tasks [16], and can, to some extent, also suggest new research ideas and summarize their findings [17]. In chemistry, they combine web search, specialized simulation tools, and access to laboratory interfaces to, for example, optimize chemical reactions [18], and synthesize molecules [19, 20]. In biology, agentic LLMs are employed to find gene perturbations resulting in specific phenotypes [21], and design gene-editing experiments [22].

In physics, non-agentic LLMs have been used to solve well-defined tasks such as calculating Hartree-Fock Hamiltonians [23] or answering questions about astrophysics [24]. Additionally, their performance has been tested on a suite of benchmarks containing typical exam questions ranging from high school to Olympiad-level difficulties [25–27], as well as on typical scientific coding tasks [28].

While exploring the capabilities of agentic LLMs in physics has been called for [29, 30], previous work focuses on building specialist agents with specific tools for tasks that require adaptability but typically follow a structured blueprint. Examples include density functional calculations [31], cosmology calculations [32, 33], calculating properties of topological materials [34], inverse design for meta-materials [35], designing integrated photonic circuits [36], and cooling of trapped atom experiments [37].

In this work, we will explore how tool use can enable an LLM to automate the heuristic loop of scientific discovery, including selecting experiments, analyzing results, and forming hypotheses when exploring an unknown system. To create a generalist agent applicable to a wide range of scenarios, we do not tailor it to a concrete system or task, i.e. we do not provide specific instructions and tools, but merely a basic description of the problem (e.g. ‘This is a physical system governed by an ordinary differential equation. Can you discover its equation of motion?’) and a simulator useful for a wide range

* maximilian.naegele@mpl.mpg.de

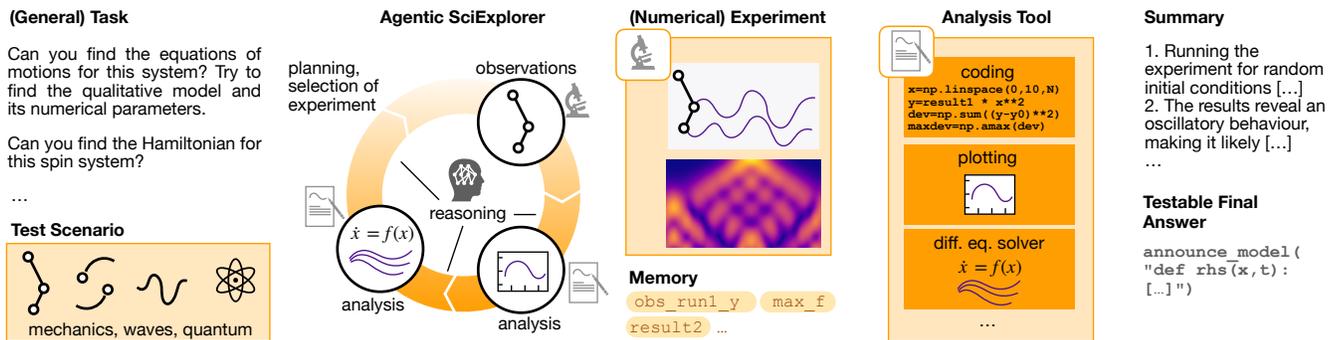


FIG. 1. **Agentic SciExplorer**. The explorer is given a general task, which is then applied to a specific physics scenario. During the scientific exploration cycle, LLM-based reasoning is employed to select a (numerical) experiment to be carried out, calling the appropriate tool. The resulting observations are analyzed using one or several calls to analysis tools, often involving both the coding and the multimodal capabilities of the LLM. This cycle repeats until the LLM agent decides it has acquired sufficient information. Finally, a summary of the reasoning chain is produced for the human user. For benchmarking, the agent is asked to provide a testable final answer, e.g. in the form of code that can be run and evaluated.

of tasks (e.g. a differential equation solver). The tools we consider include running experiments (here, numerical experiments), performing data analysis, and running simulations to test hypothetical models describing those experimental results. Based on these tools, the LLM can use its reasoning to drive an active learning process, deciding which analysis or experiment to carry out next based on previous results. We will explore in prototypical physics scenarios, drawn from fields like dynamical systems, wave dynamics, and quantum many-body systems, how this approach can successfully solve research-oriented tasks requiring heuristics by mimicking essential aspects of the scientific process. Tasks we will consider include discovering the equations of motion of a system by observing its dynamics and discovering Hamiltonians of quantum many-body systems from measurements.

Results and discussion

Agentic SciExplorer – The Agentic SciExplorer is based on an LLM agent that autonomously selects and analyzes experiments (see Figure 1), where ‘experimental’ results here are obtained via numerical simulations. In a typical scenario, the agent specifies initial conditions, observes the time evolution of a system, and adaptively selects subsequent experiments based on its previous analysis. To support this process, the agent can access several analysis tools. Rather than providing narrowly defined, user-specified tools, we leverage the advanced coding capabilities of modern LLMs [28], giving the agent access to a coding tool that executes arbitrary Python code. This choice maximizes flexibility and enables dynamic tool creation by the agent during runtime. Additionally, the agent can access a code-based plotting tool, which, paired with the agent’s multimodal capabilities, enables the agent to quickly grasp qualitative insights about the system under study by visual inspection. We integrate an external memory that is accessible through the coding and analysis tools, to offer reliable persistence of experimental and analysis results in the

form of arrays of numerical values. When addressing a user-defined task, the agent proceeds in multiple steps. Each step involves verbal reasoning and may include multiple tool calls for controlling the experiment and analyzing results. The tool results are then communicated to the agent and added to the memory (see Methods and Supplemental Material for a more complete description).

To explore the intrinsic capabilities of state-of-the-art LLMs in successful agentic exploration, we deliberately keep any domain-specific input to a minimum. The relatively short system prompt only provides general advice for scientific exploration (like systematically formulating hypotheses) but does not contain task-specific or even domain-specific information and is applied across all domains explored in the following (see Supplement S 2). In addition, we probe a general task description that can be applied across diverse physical domains, such as mechanical, wave, and quantum systems (‘Can you find the equations of motion of this system?’). Necessarily, the tool executing experimental runs depends on the scenario, but in its documentation accessible to the LLM it does not reveal anything more specific about the domain than what is absolutely needed, e.g. that the available experiment will run the dynamics of a given number of particles. Apart from that, in each of the three wide-ranging domains considered below, we supplied only one domain-specific but generic simulator for analysis, e.g. for solving ordinary differential equations in the case of mechanical systems.

If not otherwise specified, we use GPT-5 Pro [38] as the state-of-the-art LLM backbone of the SciExplorer.

Mechanical Systems – Mechanical systems provide an ideal testbed for the SciExplorer due to their wide diversity spanning conservative, dissipative, and driven regimes, and the wide range of accessible complexity levels, selected via choosing the equations of motion or their dimensionality. An example of an illustrative exploration

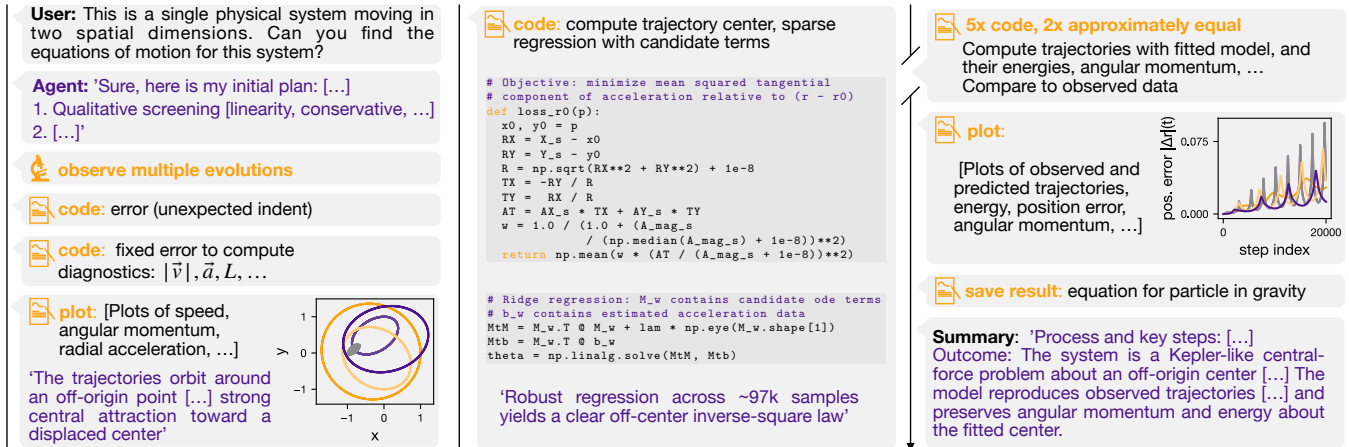


FIG. 2. **Example exploration.** The agent is tasked with discovering the unknown equations of motion of a system by observing and analyzing its dynamics. In this figure, we sketch in a compressed fashion some of the steps in the resulting extended autonomous exploration. The agent first runs several experiments with varying initial conditions. Then, it infers the qualitative model (here, a particle in some attractive potential) from visualizations. It subsequently employs fitting routines to determine the center of attraction by numerically maximizing the radial acceleration and determines the coefficients of a gravity model through sparse linear regression of the acceleration. Finally, it computes diagnostics, such as the energy and angular momentum, to validate the proposed model before saving the final result as a Python function representing the equation of motion. The sequence of steps depends entirely on the choices of the agent, which are adapted to the given problem, reacting to its own observations and conclusions.

process is summarized in Figure 2.

For test purposes, we considered generic dynamical systems with up to three generalized coordinates and systems with particles moving in 2d (with up to ten particles) subject to fixed potentials or pairwise interactions (for the full equations of motion see Supplement, Table S1). Figure 3 summarizes the agent’s performance across these systems when asked to infer their equations of motion. To quantify the agent’s performance, we compute the coefficient of determination R^2 between the right-hand side (rhs) of the differential equation proposed by the agent and the ground-truth dynamics.

As an expanded challenge, we also consider dynamical systems where the agent is only allowed to observe a subset of particles, and is not even told the number of unobserved particles. In those cases, we additionally require the agent to infer the initial conditions of the hidden particles. We then report the mean R^2 value across trajectories with random initial conditions of the observable particle (see Methods for details).

For a large subset of systems, the agent recovers the governing model both qualitatively and quantitatively, often achieving perfect fits ($R^2 \approx 1$) using only observations of the system’s time evolution under initial conditions selected by the agent. Performance degrades for more complex or atypical systems, and the agent only sometimes recovers the correct model. Systems that are not close to any known models (e.g. the ‘arbitrary 2d potential’) are particularly challenging, indicating that the LLM agent relies on its broad knowledge base to be suc-

cessful for other systems. To identify systems correctly in most cases, the agent autonomously implements a broad repertoire of analysis techniques by generating and executing Python code, without requiring specific tools. Typically, the agent first extracts qualitative signatures from visualizations. These include, among others, linearity, mirror symmetry, limit cycles, attractors, and decay. It then constructs candidate basis terms for the governing differential equations and fits their coefficients to the observed accelerations. When applicable, it uses sparse linear regression [39]. Otherwise, it fits numerical solutions of the proposed differential equations directly to the experimental data. Depending on the task, the agent uses a large set of additional strategies, such as locating centers of attraction in 2d by maximizing the radial acceleration with respect to a candidate center, testing for angular momentum and energy conservation, and using Fourier transforms to find initial parameter guesses for oscillator systems or to infer the number of hidden particles in partially observed systems.

Common failure modes of the agent include premature commitment to a set of models without reconsidering when fits are poor and overlooking qualitative cues visible in plots such as periodic oscillations in acceleration plots (for an example, see Supplement S 5 C).

Furthermore, we test the agent’s ability to self-critique by asking it, for each mechanical system, to identify in which of multiple conversations it performed best (stars in Figure 3). When the correct model was found at least once, the agent reliably selects that conversation. However, when none of the proposed models was exactly cor-

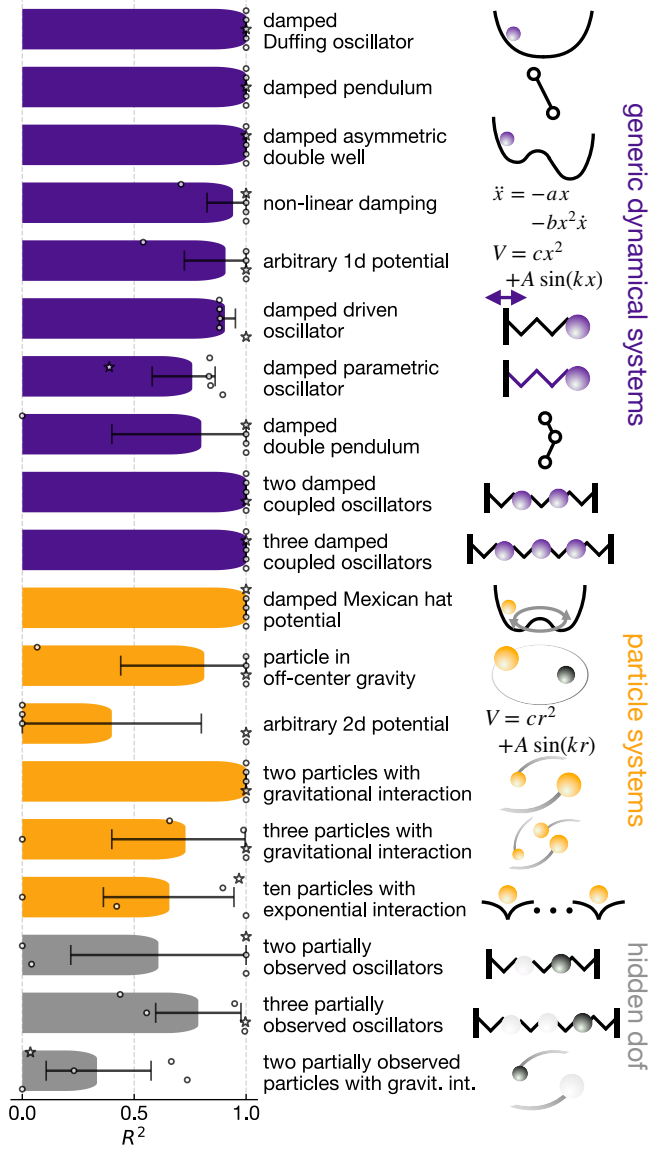


FIG. 3. **Mechanical Systems.** The agent discovers the equations of motion of black-box physical systems by specifying initial conditions, observing dynamics, and analyzing the results. We consider generic dynamical systems with one to three generalized coordinates, particles moving in 2d, and systems where an observable particle interacts with an unknown number of hidden degrees of freedom (dof). We run 5 independent attempts per system and show the mean coefficient of determination R^2 of the agent’s proposed model with the true system with 95% bootstrap confidence intervals. The agent can recover the true model in a large subset of systems. Stars indicate the conversation the agent considers best when asked to rank all attempts.

rect, the agent often does not choose the conversation corresponding to the highest R^2 value. Instead, it tends to prioritize qualitative agreement, such as the existence of bound and unbound trajectories, over purely quantitative fit quality.

It is important to note that even in a real experimental setting, one can verify the quality of the solution discovered by the agent without knowing the ground truth by comparing the agent’s theory with new experimental data. Therefore, one can boost the effective success rate of the agent by running several explorations and picking the best-performing model (in all but two of the scenarios of Figure 3, this leads to the correct solution, as it is among the five runs).

To understand which components of the SciExplorer are essential, we perform ablation studies. Depending on the physical system, both the plotting and coding tools are crucial for consistent performance. To test the importance of tool access, we compare a given exploration run of our agent against a conversation where an LLM without access to tools is initially provided with visualizations for the same number of experiments, but now with randomly chosen initial conditions. In this case, the LLM cannot recover the correct model. Interestingly, we also find that GPT 5 pro [38] performs much better than Gemini 2.5 pro [40] (for details see Supplement S1).

The superior performance of LLM agents based on state-of-the-art reasoning models relies on significant runtime investment. For the systems studied here, a single exploration ranges from a few minutes to over 1.5 hours, with the bottleneck being the LLM’s response time, not the numerical simulations of the system. We also observe that the agent generally requires more time to solve more complex systems than simpler ones (see Supplement, Figure S2). Nevertheless, based on our experience as working theoretical physicists, we estimate that the overall runtime for a single task is already lower than what even an expert human would typically need for such an initially completely open exploration of an unknown system.

Dynamics of Waves and Fields – A fundamental cornerstone of the physical description of nature is the notion of dynamics of many degrees of freedom arranged in an extended space, with locality and translational invariance as guiding principles. These lead naturally to the evolution equations of fields and waves, which also form the basis of the most fundamental theories we have. We ask the LLM agent to explore this domain by providing access to ‘experimental’ runs where the agent can set up an arbitrary initial configuration of a field ϕ and observe the subsequent dynamics $\phi(x, t)$ that is governed by a classical evolution equation unknown to the agent. The agent may aid its analysis by running simulations for arbitrary hypothesized field equations. In the present incarnation of this scenario, we specialized to 1d field equations (with correspondingly lower numerical effort for a single run) for a complex field ϕ . Examples that we tested the agent on include the nonlinear Schrödinger equation, describing the dynamics of matter waves of interacting atoms or light waves subject to nonlinearities, and the time-dependent Ginzburg-Landau equation, describing the evolution of an order parameter field, e.g. in

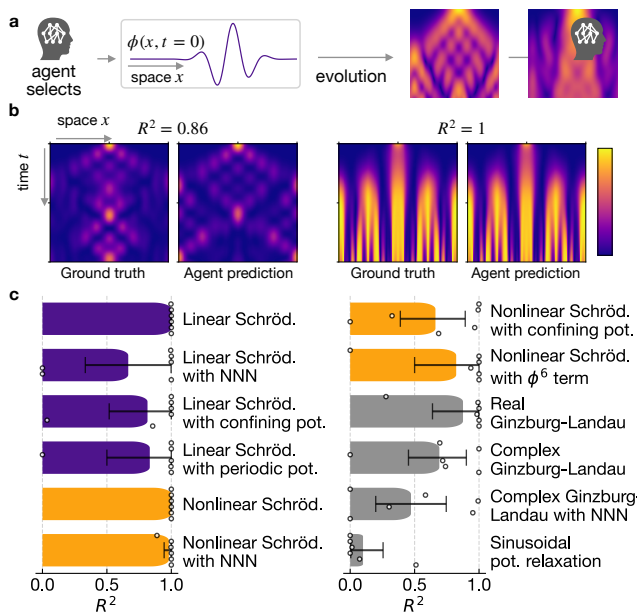


FIG. 4. **Waves and fields.** **a** In its exploration of waves and fields, the agent can select the initial field configuration for each experimental run. It can also define and simulate field equations for comparison. **b** Evolution of the absolute square $|\phi|^2$ of a Gaussian wave packet for the true model and the agent’s discovered model (announced by the agent at the end of the exploration). The true model on the left is a linear Schrödinger equation with confining potential (we do not show the most accurate model discovered by the agent in its multiple runs). On the right, the true model is a complex Ginzburg-Landau equation with next-nearest-neighbor hopping on a tight-binding lattice. The R^2 value is calculated between the evolution equations for the true and the predicted model, for multiple reasonable initial conditions (see Methods for details). **c** Statistics for various scenarios. We run six independent explorations, and the agent can recover the true model ($R^2 \approx 1$) in all but one scenario in at least one attempt.

a superconductor, relaxing to its thermodynamic equilibrium configuration. In each case, there can be variations like the presence of an arbitrary external potential or of longer-range coupling terms on the underlying lattice. The SciExplorer can discover the true model for any of these variations when given multiple attempts (see Figure 4). However, it struggles with an artificial model describing relaxation into a sinusoidal potential for the field.

In all field and wave scenarios, we provide the same simulation tool to the agent, which requires the agent to spell out its hypothesized evolution equation in Python code. This code defines the local evolution in x -space (including any nonlinear and potential terms) and the evolution in k -space (the kinetic part, including wave propagation or diffusion). These components can be directly used within a split-step integrator. The agent performs very well in translating back and forth between the evolution equa-

tion itself (e.g. $\partial_t \phi = -i\Delta\phi - ig|\phi|^2\phi$), which it mentions in its analysis, and the corresponding Python specifications that also account for lattice dispersion.

In our studies, we observe that the agent often lays out a detailed exploration plan in advance, mentioning the most important field theories as plausible options, sometimes including expected signatures, such as Bragg scattering for linear waves in periodic potentials or soliton-like features for Kerr-type and other nonlinearities. It tends to start with a Gaussian wave packet as its choice of initial condition in the first experiment. If the results of this experiment indicate wave-like dynamics, the agent often adopts a principled approach where it first tries to extract the dispersion relation. One of its strategies is to launch several plane waves of varying wavenumber and low amplitude to avoid nonlinearities, and to analyze the evolution of the phase of the field ϕ . Once that is settled, it tries to determine any nonlinearities by checking the amplitude dependence of the evolution. If the initial dynamics are not wave-like but contractive, with dissipation leading to some steady state, it will adapt its strategy accordingly. In both cases, the agent often visualizes the field $\phi(x, t)$ using space-time density plots, e.g. with the declared aim to ‘spot qualitative structures (breathers, oscillations, solitons)’. Using these strategies, we find it to quickly make systematic progress (see Supplement S5D for an example).

Quantum Many-Body Physics – In domains ranging from condensed matter physics to particle physics, the fundamental language is that of quantum many-body systems. The essence of this domain, with complexities like the exponential growth of the Hilbert space with particle number and the presence of entanglement, is captured well by models of interacting spins or qubits. We therefore let the agent explore and analyze spin Hamiltonians, a task with wide-ranging applications from solid-state physics to quantum technologies [41, 42]. In terms of experiments, we test two variations: (i) In one setting, the agent can initialize the system in a product state and then observe the temporal evolution of the expectation values of single-spin operators. (ii) In another setting, the agent can construct arbitrary observables (Hermitian operators) and obtain their expectation values in the ground state of the unknown Hamiltonian (see Figure 5). As usual, the agent is also provided with a tool that can set up a freely chosen many-spin Hamiltonian and either simulate its time dynamics or get its ground state expectation values, respectively. The agent is told that it may specify the Hamiltonian or the operators via Python code that is given access to the predefined spin operators.

We find that the agent has an active working knowledge of quantum many-body physics and spin models in particular, including standard models like transverse Ising, XXZ, and Heisenberg, but also e.g. Dzyaloshinskii-Moriya (spin-orbit induced) chiral couplings. It can deploy that knowledge reliably in this challenge.

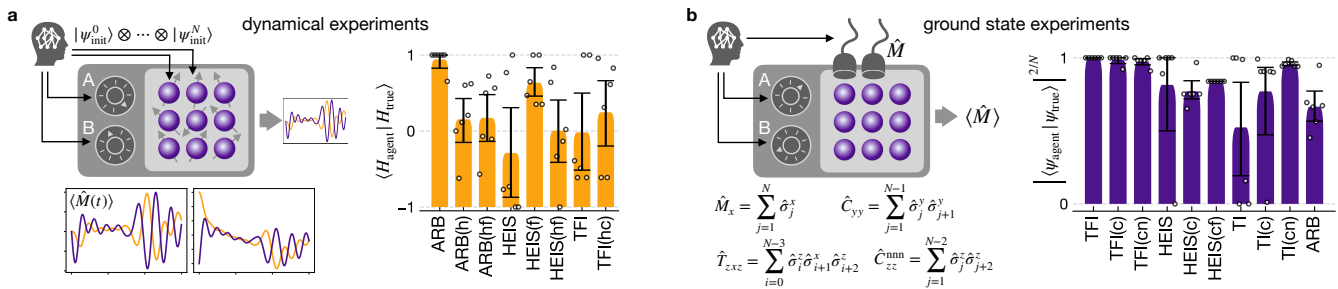


FIG. 5. **Quantum Many-Body Physics.** **a** Discovering the Hamiltonian of a system of multiple spin-1/2 particles, based on observing the dynamics for initial conditions selected by the agent. Each experimental run produces the evolution of the single-spin expectation values $\langle \hat{M}(t) \rangle$ (with $\hat{M} = \hat{\sigma}_j^x$, $\hat{\sigma}_j^y$, and $\hat{\sigma}_j^z$), for an initial (product) state selected by the agent. In some experiments, we ask the agent to discover a whole class of Hamiltonians by allowing it to control experimental parameters, whose meaning it is not aware of ('A' and 'B'). The bottom left shows an example – the complex dynamics of two spins of a Heisenberg model. Right: Performance for various scenarios. Normalized scalar product between the true Hamiltonian and the Hamiltonian proposed by the agent (1 means perfect match, for details see Methods). We consider the following systems: *ARB*: Arbitrarily chosen Hamiltonian acting on 3 spins, *HEIS*: 1d Heisenberg model with 10 spins (in two of the attempts, the agent actually discovered the correct model but made a formal error when announcing the final Hamiltonian; we counted them as overlap -1), *TFI*: 1d transverse field Ising model with 10 spins. The letters in brackets denote whether the agent can vary the value of a field parameter (f), of a coupling parameter (c), or observe only two spins of a larger chain (h). **b** Hamiltonian discovery by measuring the ground state expectation values of spin operators \hat{M} defined by the agent. Some examples are shown on the bottom left. Right: Fidelity scaled by the number of spins N between the ground state of the Hamiltonian predicted by the agent after the exploration and the true ground state. We consider the following systems: *TFI*: 1d transverse field Ising model with 10 spins, *HEIS*: 2d Heisenberg model with 9 spins, *TI*: 1d topological Ising model with three-body interactions and 10 spins, *ARB*: Arbitrarily chosen Hamiltonian acting on 3 spins. Letters denote the same as in part a. Additionally, the agent can sometimes vary the number of spins in the chain, as denoted by (n).

For the dynamical setting, where the time traces of spin expectation values can look very complex, the agent can nevertheless quickly rule out some hypotheses. For example, it may run short-time dynamics for multiple initial states, which allows it to first check for conserved quantities such as the global magnetization, compute dominant frequency components using Fourier transforms, and discriminate local and many-body interactions. It then often obtains fits to hypothesized families of Hamiltonians (for an example, see Supplement S5F). We also introduced an even more challenging scenario, where the agent can only observe and control a subset of spins. As expected, this appears to be one of the most complex tasks, and the agent only sometimes makes good progress. For example, in one attempt to discover a ten-spin Heisenberg model by observing only two spins, the agent correctly identifies a tunable field in the X direction but mistakes the coupling to be of XY- instead of Heisenberg-type.

In the ground state setting, the agent typically first probes the symmetry and structure of the Hamiltonian by selecting a limited set of intelligently chosen operators, obtaining single-spin expectation values as well as nearest-neighbor correlators but also more subtle quantities suited e.g. for exploring potential chirality, like $\langle \hat{S}_x^j \hat{S}_y^{j+1} - \hat{S}_y^j \hat{S}_x^{j+1} \rangle$. It quickly deduces aspects like open boundary conditions, translational invariance, and the likely absence of some families of spin-coupling terms in the Hamiltonian. It then selects candidate spin Hamil-

tonians, conjectures values of their parameters, and runs the simulation tool to confirm or reject these hypotheses. The agent is also cautious enough to keep an open mind (as per its instructions) and lists possibilities that have not yet been refuted, like more subtle, longer-range couplings.

In an extension to both the dynamical and ground-state setting, we let the agent control one or several parameters whose meaning it is unaware of (mimicking closely a potential experimental scenario of exploration), letting it discover a whole family of Hamiltonians. Here, the agent sometimes struggles with specifying the correct scaling or sign of the tunable parameter. For example, in the 2d Heisenberg model with varying coupling and field, it correctly identifies the Hamiltonian structure but misses a factor of two in all six explorations. However, we find that the agent can also successfully solve this extended task for many of the other considered systems by, for example, creating visualizations of expectation values against the strength of the tunable parameters (for an example, see Supplement S5E).

Overall, as demonstrated in Figure 5, the agent also performs impressively well in discovering models in quantum many-body physics, again without any fine-tuned instructions or a prescribed exploration loop.

Conclusion

We have demonstrated that SciExplorer can successfully address open-ended, research-style tasks by interacting

with physical systems through repeated cycles of experimentation and analysis. The LLM at the core of SciExplorer leverages broad knowledge across diverse areas of physics, such as classical mechanics, wave dynamics, and quantum systems, to autonomously characterize systems in a single-shot manner, i.e. without example solutions and with only minimal task- or system-specific instructions. Equipped with generic, code-based analysis and visualization tools, the agent can implement an active learning process to solve tasks such as discovering equations of motion from observed dynamics and recovering Hamiltonians, or even Hamiltonian families, from expectation values.

In physics, many modern experiments are controlled through code-based interfaces, which makes SciExplorer directly applicable in experimental settings such as complex fluids, cold atomic gases, strongly correlated electronic and spin systems, or quantum simulators. While model discovery remains highly relevant in these systems, SciExplorer could, for example, also map out phase diagrams or optimize control tasks in unknown or partially known systems.

The iterative process of experiment selection, analysis, and hypothesis generation is not unique to physics but lies at the heart of the natural sciences more broadly. Because LLMs possess substantial knowledge across scientific domains such as chemistry [43, 44] and biology [45, 46], and because SciExplorer requires no task-specific fine-tuning, applying this framework to other scientific fields is a natural next step, for example, to study predator-prey dynamics in biology or chemical non-equilibrium dynamics.

Methods

SciExplorer – After supplying the generic and rather brief system prompt (identical throughout all experiments), the LLM agent receives a short description of the problem class (e.g. a dynamical system or a spin system) and the task (e.g. discovering equations of motion or the Hamiltonian). In addition, as for any application of agentic tool use, the LLM has access to the documentation of the tools it can access. To facilitate the efficient integration of new analysis tools and experiments into the SciExplorer framework, we automatically generate OpenAI API-compatible documentation by parsing the docstrings of tool methods. We list all such inputs to the LLM (prompts, problem class description, task description, tool documentation) in the Supplementary Material.

In the following steps of the automated conversation, the agent only receives a hint about the number of remaining conversation steps and tool calls, and a reminder to heed the system prompt.

In all explorations, the agent has access to three generic core tools: `execute_code` for executing generic Python code, `plot_from_code` for creating Matplotlib plots, and `approx_equal` for receiving a verbal assessment of the

similarity of two lists of numerical values, as we observed that this reduces the agent’s overconfidence when comparing candidate models to ground-truth data. Beyond these, the only additional analysis tools are simulators, which differ across the broad domains considered in this manuscript (see below).

The results of each tool call of the agent are saved to the external memory under a result label, which the agent is automatically asked to specify to enable descriptive names. These results are then accessible as local variables in the `execute_code` and `plot_from_code` tools. The tool results are also communicated to the agent as plain text in case of arrays with fewer than 10 entries. Otherwise, only the shape of the array is supplied to avoid the need for unnecessarily large context windows. If a tool results in an image, it is supplied back to the agent for visual inspection.

The agent can choose to finish the exploration at any time, and it is then asked to announce its result in the form of Python code that defines the solution hypothesized by the agent (see below).

After a given run of the agent, we save the entire conversation for further inspection.

Mechanical systems – We use a differential equation solver to solve the equations of motion, both for the ‘experimental’ runs of the system that is unknown to the agent, and as a possibility for the agent to simulate hypothesized equations of motion (accessible as a function within the ‘code’ tool). To run an experiment, the agent can specify initial conditions to receive generalized coordinates and velocities of the system evaluated on a time grid using the `observe_evolution` tool. We allow the agent to observe up to 5 experiments within a single tool call to reduce the steps needed to explore the system. When using the differential equation solver during analysis, the agent is asked to provide code computing the right-hand side (rhs) of the ordinary differential equation. For example, the code for a damped pendulum would read:

```
def rhs(X,t):
    l, gamma = 1.712, 0.05
    return jnp.array([X[1], -1*jnp.sin(X[0]) -
                    gamma * X[1]])
```

When the agent is finished with its explorations, it submits the hypothesized equations of motion of the unknown system as Python code for the right-hand side in the format used above.

To evaluate the performance of the agent, we require a single continuous value describing how ‘close’ the agent’s prediction is to the truth. We estimate the coefficient of determination

$$R^2(\vec{x}, \vec{y}) = 1 - \frac{\sum_i (x_i - y_i)^2}{\sum_i \left(\sum_j x_j - x_i \right)^2}$$

between the true (\vec{x}) and predicted (\vec{y}) rhs function by sampling 1000 random position-velocity-time combinations. We then compute R^2 for each coordinate and velocity separately and average them to obtain a single metric. The R^2 value can range from $-\infty$ (bad fit) over 0 (as good as predicting $\vec{y} = \text{mean}(\vec{x})$) to 1 (perfect fit). Therefore, we lower-bound this value by zero to enable reasonable averaging of multiple runs. For partially observable systems, this method is not applicable due to two reasons: First, the agent might predict a rhs of different dimensionality than the true rhs. Second, for correctly predicting the dynamics, the initial conditions of the hidden particles also need to be determined. Therefore, we ask the agent to provide these in addition to the rhs function. We then simulate 100 trajectories with both the true dynamics and the agent’s prediction with random initial conditions of the observed particles. Finally, we compute the mean R^2 of the trajectory of the observed particle between the true and predicted dynamics, i.e. we ask the agent to reproduce the observed dynamics, but don’t require it to correctly reproduce the hidden dynamics.

Fields and waves – We set up a split-step integrator for the evolution of a complex field ϕ on a 1d lattice, providing the ‘experimental’ results for a hidden evolution equation with initial conditions specified by the agent using JAX code [47] (`run_field_evolution_experiment` tool).

For analysis, the agent can simulate a proposed model by first using the `set_field_rhs` tool to provide an evolution equation in the form of Python code that can be run inside the split-step integrator, separating x -space and k -space evolution. For the example of the nonlinear Schrödinger equation with unit coefficients, this code reads:

```
def U_kinetic(phi_k,k,t,dt):
    return jnp.exp(-1j*(1-jnp.cos(k))*dt) *
        phi_k

def U_potential(phi,x,t,dt):
    return jnp.exp(-1j*dt*jnp.abs(phi)**2) * phi
```

We found this way of allowing the agent to specify the field evolution the most suitable for our purposes, since it offloads the translation from the evolution equation $\partial_t \phi = \dots$ to the actual code to the agent, and as in all coding tasks, the agent performs very well in this challenge. We ask the agent to employ `jax.numpy` code, since that meshes well with our GPU-accelerated simulation code. To start a simulation, the agent can use the `run_field_simulation` tool to specify an initial condition and observe its dynamics under the previously defined evolution.

To evaluate the performance of the agent, we proceed as follows: We first run the wave evolution for different reasonable initial conditions (multiple Gaussian wave

packets with and without momentum and with different amplitudes) to obtain a large set of physically relevant field/wave functions $\phi(x,t)$. We then numerically calculate $\frac{d\phi(x,t)}{dt}$ for all initial conditions and all times t under both the true model and the agent’s prediction and calculate the R^2 value between them.

Quantum many-body physics – We consider a system of N spin-1/2 degrees of freedom (qubits). We predefine the Pauli matrices \hat{S}_x^j , \hat{S}_y^j , and \hat{S}_z^j . These matrices can be used to define Hamiltonians or operators to observe. An example of such code looks like the following, for the transverse quantum Ising model:

```
H=0*Sz[0]
for j in range(10):
    H+=Sx[j] @ Sx[j+1]
for j in range(10):
    H-=0.5*Sz[j]
```

Depending on the scenario, the agent can either retrieve ground state expectation values of previously specified operators (using the `set_operator_for_ground_state` and `run_experiment_ground_state` tools) or observe the dynamics of a (hidden) Hamiltonian by specifying an initial product state of the spins (`run_experiment` tool). In the latter case, we also consider a more challenging scenario in which the agent is only allowed to observe and initialize a selected subset of spins, while all other spins are set to a default state in each experimental run.

For both ground-state and time-dependent experiments, we also consider scenarios where the Hamiltonian depends on one or more tunable parameters (as in $\hat{H} = \sum_j \hat{\sigma}_j^x \hat{\sigma}_{j+1}^x - A \sum_j \hat{\sigma}_j^z$), which the agent can set before running an experiment. This allows model discovery of a whole parametrized family of Hamiltonians. In a variant of this scenario, the agent may also choose the number N of spins in the experimental system, e.g. to explore finite-size effects in translationally invariant models.

For analysis, we provide additional simulator tools to the agent. The agent can define hypothesized Hamiltonians (`set_Hamiltonian`) and, for the ground state tasks, propose operators (`set_operator`) in a similar manner as above. It can then evaluate expectation values using the `get_ground_state_expectation` tool by specifying the labels of previously defined Hamiltonians and operators. For the time-dependent dynamics, the agent can instead use the `init_spins` tool to initialize the spins in a product state by specifying their Bloch vectors. To run a dynamics simulation, the agent can specify the labels of previously defined Hamiltonians and initial states (`solve_SEQ` tool).

In the ground-state experiments, we evaluate the agent’s performance by calculating the fidelity per spin between the ground state predicted by the agent and the true ground state, i.e. $|\langle \psi_{\text{agent}} | \psi_{\text{true}} \rangle|^{2/N}$, where N is the number of spins in the system. This quantity is defined so as to become system-size independent in the thermody-

dynamic limit of large N . For the dynamics tasks, we first shift the Hamiltonians by $H'_i = H_i - \text{tr}(H_i)/2^N$ and then compute the scalar product of these shifted Hamiltonians as $\text{tr}[(H'_{\text{true}})^\dagger H'_{\text{agent}}] / \max(\|H'_{\text{true}}\|, \|H'_{\text{agent}}\|)^2$, where $\|\cdot\|$ denotes the Frobenius norm $\|A\| = \sqrt{\text{tr}[A^\dagger A]}$. Taking the maximum of both norms in the denominator ensures that multiplying the predicted Hamiltonian by a scalar, thereby effectively rescaling time, results in a lower quality score. For tasks with tunable parameters, we average the quality score over 100 random values of these parameters.

Data and code availability

The complete SciExplorer framework, including documentation on adding new experiments and analysis tools, is available as a Python package on GitHub [48]. Additionally, we provide all code used to run the explorations presented in this manuscript, logs of all explorations, and tools to print or summarize those explorations in a second GitHub repository [49].

Acknowledgments

This research is part of the Munich Quantum Valley, which is supported by the Bavarian state government with funds from the Hightech Agenda Bayern Plus.

Supplementary Material

S1. ESSENTIAL INGREDIENTS OF THE SCIEXPLOERER

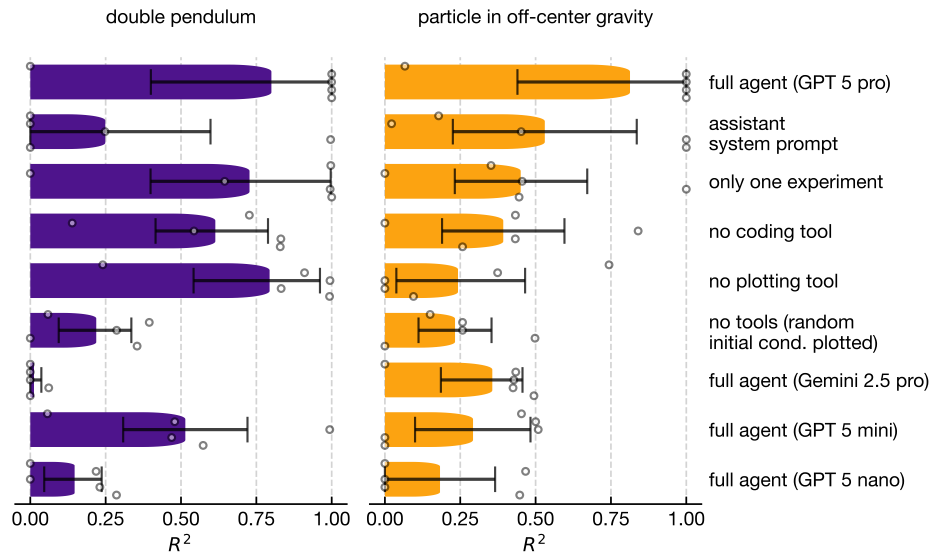


FIG. S1. **Ablation studies.** Mean performance of the agent in the double pendulum and the particle in off-center gravity task with different modifications. Error bars are 95% bootstrap confidence intervals. *Full agent (GPT 5 pro)*: Original SciExplorer with GPT 5 pro [38] as an LLM backbone. *Assistant system prompt*: Changed system prompt to 'You are a helpful assistant'. *Only one experiment*: Agent can observe only one trajectory. *No coding tool*: Agent cannot execute arbitrary Python code, but only plot experimental results. *No plotting tool*: The agent cannot generate visualizations. Instead, down-sampled experimental trajectories are stored in the agent's context. *No tools*: The agent cannot use any tools. In the beginning, it is instead provided with time evolution and phase space plots of multiple trajectories with random initial conditions. *Full agent (Gemini 2.5 pro)*: Original SciExplorer with Gemini 2.5 pro [40] as an LLM backbone. *Full agent (GPT5 mini)*: Original SciExplorer with GPT5 mini as an LLM backbone. *Full agent (GPT5 nano)*: Original SciExplorer with GPT 5 nano as an LLM backbone.

To assess which components of the SciExplorer are essential, we performed ablation experiments on two representative systems: the double pendulum and the particle in off-center gravity (Figure S1). The relative importance of individual components differs between these systems. A structured system prompt appears to improve performance in both cases, whereas access to multiple experiments and visualization tools is particularly critical in the gravity system. Without the coding tool, the agent sometimes recovers the correct qualitative model but consistently fails to identify accurate numerical parameters. Without any access to tools and instead provided with plots of trajectories under random initial conditions (matching the number of experiments selected by the full agent), the LLM is unable to identify accurate models.

Finally, we observe substantial variation across LLMs: GPT 5 Pro [38] dramatically outperforms Gemini 2.5 Pro [40], which fails to recover the true models even when granted access to the full SciExplorer framework. Similarly, GPT5 mini and GPT5 nano fail to find the true models in all attempts but one.

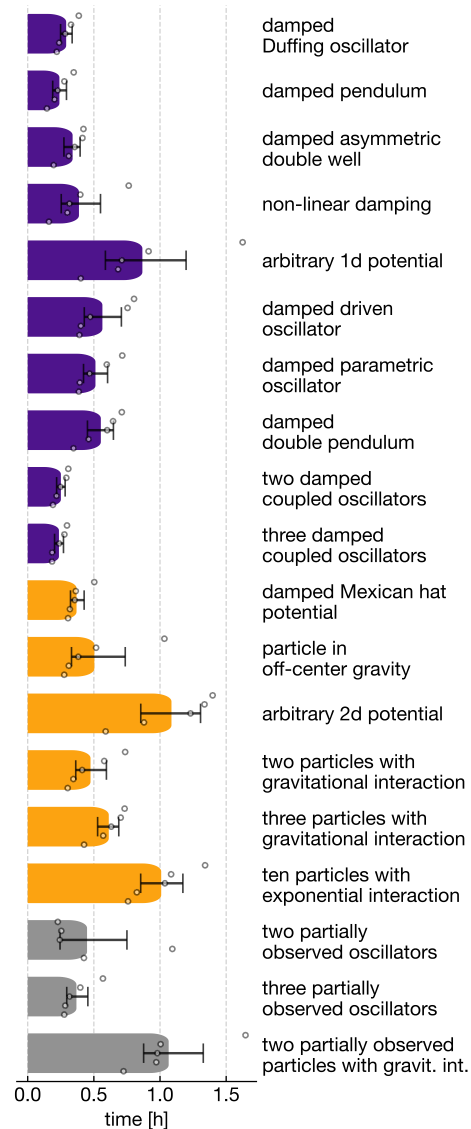


FIG. S2. **Runtime analysis.** Runtime of the classical mechanics explorations shown in Figure 3 in hours. Runtimes range from a few minutes to over 1.5 hours.

S 2. PROMPTS

Throughout all tasks and physics scenarios, we use the same generic and relatively brief system prompt, essentially instructing the LLM to act like a cautious scientist:

System prompt

- Act as a computational physicist dedicated to thoroughly resolving the user's query through careful planning, hypothesis generation, and iterative verification.
- In your first message, create a comprehensive plan to solve the users query. Include an extensive list of candidate hypotheses.
- Initially, conduct at least 5 different experiments spanning the entire range of reasonable initial conditions. Make sure to cover also extreme cases. Then, create informative plots of your experimental results.
- Withhold any final answer until you are sure that no further improvements of your hypothesis are possible.
- If you have run a tool but still need to extract the results (e.g. via visualization), just briefly explain what tool you will call next to extract the results.
- Otherwise, at each step, you must answer the following questions:

1. What can you learn from the new tool results (if any)?
2. Which old hypotheses still fit your data?
3. Which new hypotheses might be worthwhile considering?

Even though we ask the agent to answer the questions above at each step, it does not reliably do so. However, summaries of the internal thinking process of the agent indicate that it considers the questions internally. We use the following intermediate user message after each response from the agent:

Intermediate message

Keep solving the problem while following your system prompt. Make sure to answer the questions posed in the system prompt in your response.

S3. DETAILS ON ANALYSIS TOOLS

For all tasks and scenarios, we provide the following generic analysis tools to the agent, exploiting the proven power of LLMs in coding. We here display the documentation strings, which are the only information available to the LLM agent:

Analysis: code-based plotting

```
def plot_from_code(code: str):
    Execute python code that produces a plot from one or more previously saved arrays.
    The following variables are available during evaluation:
        all previously saved fields with their previously stated result_labels as variable
        names.
        get_image: function to get the image of the plot.
    You may import the following libraries:
        matplotlib: for plotting.
        matplotlib.pyplot as plt: for plotting.
        jax: for numerical operations.
        jax.numpy: for numerical operations.
        numpy: for numerical operations.
    The end of the code must say "result=get_image()" such that the image of the plot can be
    returned for visual analysis.
    Args:
        code: python code that produces a plot (without calling plt.show).
    Returns:
        Image
```

Analysis: compare two arrays

```
def approx_equal(a1:jax.Array, a2:jax.Array):
    Check whether two arrays can be considered approximately the same.
    This calculates their mean-square error and compares it to the mean square variation.
    Args:
        a1: first array
        a2: second array
    Returns:
        statement: a string indicating the closeness of the two arrays
        ratio: (mean-square error) / max(mean square variation)
```

Analysis: code based analysis

```
def execute_code(code: str) -> dict:
    Evaluate python code.
```

```

This code can be e.g. be used to transform the previously saved fields or to
calculate or save new fields.
You cannot use this code to generate plots or images.
You cannot see print statements or other output of this code. Instead, you can use
the result variable to save the results of the code.
The following variables are available during evaluation:
  all previously saved fields with their previously stated result_labels as
  variable names (as local variables).
  jax: jax for numerical operations.
  jnp: jax.numpy for numerical operations.
  np: numpy for numerical operations.
  scipy: scipy for numerical operations including optimization and solving
  differential equations.
  optax: optax for efficient gradient based optimizers like adam, rmsprop, etc.
Additionally, you have access to an ode solver with the following signature:
def ode_solve(X0:jax.Array, rhs: callable, params:jax.Array, dt:float, T:float):
    Solve the differential equation  $dX/dt=rhs(X,t,params)$ , up to time T using the
    Runge-Kutta method, with time step dt, and initial condition X0.
    The right-hand side of the differential equation is given by the function
    rhs(X,t,params).
    Args:
        X0 (jnp.array): the initial condition, in the form of an array,
        for example "jnp.array([0.3,0.2,0.5])"
        rhs (callable): the right-hand side of the differential equation, must be
        JIT-compilable, in the following form:
            def rhs(X:jax.Array, t:float, params:jax.Array) -> jax.Array:
                <code that calculates rhs and returns the result>
            The function must return a jax.Array of the same shape as X
        params: the parameters, in the form of an array,
        for example "jnp.array([0.1,0.8])"
        dt (float): the time step size, for example 0.001
        T (float): the final time, for example 20.0,
    Returns:
        Xs (jnp.array): the solution, an array of shape (len(ts), *X0.shape)
    You can vmap the ode_solve function to solve multiple initial conditions at once.
    The code must set the variable 'result' to a dictionary in the end which should
    contain the newly generated data. E.g. result={'<result_key>': <data>, ...}.
    Args:
        code: python code that sets the result variable to a dictionary containing some
        newly generated data.
    Returns:
        the result dictionary.

```

Here, the part relating to the ode solver is only available when mechanical systems are explored.

For field or wave systems, we supply the following additional analysis tools:

Analysis: Set the right-hand side of the field simulator

```

def set_field_rhs(rhs_label:str, code: str):
    Define the right-hand side of a complex field equation to be simulated.
    The field equation will be simulated using the split-step method, applying potential
    terms in real space and kinetic terms (from spatial derivatives) in Fourier space.
    You pass a python code that must be of the form:

    def U_potential(phi,x,t,dt):
        # jax code that calculates the evolution of the
        # complex field phi for a time step dt at time t
        # and returns the result. This evolution here
        # only accounts for the terms of the field partial differential equation
        # that do not involve spatial derivatives (those
        # will be handled separately). x is a 1D array for
        # the real-space grid points.
        # Example: return jnp.exp(-1j*dt*0.1*jnp.sin(x))*phi

    def U_kinetic(phi_k,k,t,dt):

```

```

# jax code that calculates the evolution of phi_k
# from the spatial-derivative terms in the field equation,
# for a time step dt at time t and returns the result.
# phi_k is the field in Fourier space. k is a 1D array
# for the Fourier space grid points.
# Example: return jnp.exp(-1j*(1-jnp.cos(k))*dt)*phi_k
Use jax.numpy syntax in the form "jnp.exp(...)".
Args:
  rhs_label:str the label the function will be stored under.
  code:str the python code defining the evolution functions.
Returns:
  Message indicating wether the functions were set successfully.

```

Analysis: Run the field simulator

```

def run_field_simulation(rhs_label: str, initial_condition_code: str):
    Run a single field simulation, for the field evolution equation defined previously
    under rhs_label (using set_field_rhs), and for the given initial condition.
    Args:
      rhs_label: label used previously in a call to set_field_rhs
      initial_condition_code: a formula in x that uses jax syntax, i.e.
        jnp.sin(...) etc. It must define phi0, which is a complex
        array of the same shape as x.
    Returns:
      solution as a dictionary with entries
      - ts: the time points (1D array)
      - x: the x grid (1D array)
      - phis: the complex field solution,
        a 2D jax.Array of shape [n_ts,n_x]

```

For quantum many-body tasks, we additionally supply a simulator with the following tools:

Analysis: Set initial conditions of the quantum simulator

```

def init_spins(N: int):
    Set the number of spins in the system. This needs to be called before setting the
    Hamiltonian. It may be changed later if you want to run different simulations, but
    then you need to set the Hamiltonian again.
    Args:
      N: number of spins
    Returns:
      Success message

```

Analysis: Set Hamiltonian of the quantum simulator

```

def set_Hamiltonian(hamiltonian_label:str, hamiltonian_code: str):
    Define the Hamiltonian for a quantum system to be simulated.
    You pass a python code that must produce a Hamiltonian H, constructing
    it out of provided spin operators. Here Sx is a list of spin operator x-components,
    Sy likewise for the y-components, and Sz for the z-components.
    These are Pauli matrices. They can be accessed like Sx[2] etc. Remember to use the
    "@" matrix multiplication operator when taking the product of several spin operators.
    Otherwise you can use jax.numpy syntax in the form "jnp.sin(...)".
    Args:
      hamiltonian_label: the label the Hamiltonian will be stored under.
      hamiltonian_code: the python code defining the Hamiltonian.
    Returns:
      Message indicating wether the Hamiltonian was set successfully set.

```

For quantum dynamics tasks, the simulation is run with:

Analysis: Run quantum dynamics simulation

```
def solve_SEQ(hamiltonian_label: str, bloch_vectors: jax.Array, T: float, dt: float):
    Solve the time-dependent Schrödinger equation for a given fixed Hamiltonian that was
    defined previously. The initial state is given as a product state over the spins making
    up the system. The spins are spin-1/2, described by Pauli matrices Sx, Sy, and Sz.
    Args:
        hamiltonian_label: the label for the previously defined Hamiltonian
        bloch_vectors: an array (jax.Array) of shape [N,3], where N is the number
            of spins in the system, and for each spin a unit Bloch vector is prescribed
            that determines the initial direction of the spin.
        T: the time until which the equation should be solved
        dt: the time step size for the solution. nsteps will be int(T/dt)+1.
    Returns:
        'ts': jax.Array of shape [nsteps] (with the time steps 'nsteps')
        'Sx_t': jax.Array of shape [nsteps, N] with the expectation values of all
        Sx operators
        'Sy_t': jax.Array of shape [nsteps, N] with the expectation values of all
        Sy operators
        'Sz_t': jax.Array of shape [nsteps, N] with the expectation values of all
        Sz operators
```

For quantum ground state tasks, there are two analysis tools to control the simulator:

Analysis: Set operator to be observed for quantum ground state tasks

```
def set_operator(operator_label:str, operator_code: str):
    Define a Hermitian operator, whose expectation value in the ground state of a system
    can later be evaluated.
    You pass a python code that must produce an operator H, constructing it out of
    provided spin operators. Here Sx is a list of spin operator x-components, Sy likewise
    for the y-components, and Sz for the z-components.
    These are Pauli matrices.
    They can be accessed like Sx[2] etc. Remember to use the "@" matrix multiplication
    operator when taking the product of several spin operators.
    Otherwise you can use jax.numpy syntax in the form "jnp.sin(...)".
    Args:
        operator_label: the label the operator will be stored under.
        operator_code: the python code defining the operator.
    Returns:
        Message indicating whether the operator was set successfully.
```

Analysis: Obtain the expectation values of multiple operators in the ground state

```
def get_ground_state_expectations(hamiltonian_label: str, operators: str):
    Obtain the ground state expectation values of several operators.
    Args:
        hamiltonian_label: the label for the previously defined Hamiltonian
        operators: a string with a comma-delimited list of operator labels (previously
        defined via set_operator)
    Returns:
        dict containing the expectation values for each of the operators (dict key named
        according to the operator label)
```

S4. DETAILS ON PHYSICAL SYSTEMS INCLUDING EXPERIMENT TOOLS

Here, we state the governing equations of each physical system and the experimental tools available to the agent when exploring the system.

A. Mechanical systems

The agent is asked to discover the ordinary differential equation describing a physical system by observing its dynamics. Depending on the system type, we provide different descriptions of the system, experimental tools, and tools to save the predicted differential equation, as listed in detail below.

In short, for the generic dynamical systems, the agent is told their dimensionality, but coordinates are called 'generalized coordinates' and do not have descriptive names. For the systems with particles moving in 2d, the agent is told the number of particles and that they move in 2d. For the systems with hidden degrees of freedom, the agent is told that it can observe a particle moving in 1d/2d interacting with an unknown number of unobserved particles that start with the same initial condition in each experiment. In addition, the agent is told a reasonable range of coordinates for each experiment. For the exact equations of motion governing each system, see Table S1. For each system, we provide a tool to observe the dynamics of the system given agent-specified initial conditions (displayed below) and a second tool where the agent can instead pass a list of up to 5 initial conditions to observe multiple trajectories with one tool call (not displayed below). The exact equations of motion of the systems are listed in Table S1.

1. Generic dynamical systems

This sections contain the description of the system and tools provided to the agent for the generic dynamical systems (damped Duffing oscillator, damped pendulum, damped asymmetric double well, non-linear damping, arbitrary 1d potential, damped driven oscillator, damped parametric oscillator, damped double pendulum, two damped coupled oscillators, three damped coupled oscillators).

Description supplied to agent for generic dynamical systems

This is a physical system governed by an ordinary differential equation.

In the following, we show the experiment tools for systems with two degrees of freedom. For systems with a different number of degrees of freedom, we slightly adapt the tools. We also adapt the range of reasonable coordinates for each experiment (see Table S1). In case a tool description describes multiple coordinates equivalently, we abbreviate using [...].

Experiment: observe evolution given initial conditions for generic dynamical systems

```
observe_evolution(q0: float, q1: float, q0_dot:float, q1_dot:float,)
    Observe a trajectory of the system given initial conditions.
    A reasonable coordinate range is e.g. (-1, 1).
    Args:
        q0: first generalized coordinate
        q1: second generalized coordinate
        q0_dot: first generalized velocity
        q1_dot: second generalized velocity
    Returns:
        'ts':jax.Array of shape [nsteps] with the time steps
        'array':jax.Array of shape [nsteps,dimension] with the solution,
                array[:, 0] holds the first generalized coordinate
                [...]
```

The agent is asked to save its final prediction using the following tool:

Save predicted equation of motion

```
save_result_find_eom(rhs: str):
    Compare the provided right-hand side of the ordinary differential equation with the
    true right-hand side governing the differential equation of the system.
    The loss is computed as the mean squared error between the true rhs
    and predicted rhs at some randomly sampled points.
    This tool should only be used to provide the final result.
```

```

It can only be called once per experiment.
Args:
  rhs: Define the right-hand side of an ordinary differential equation.
        You pass a python code that must be of the form
        def rhs(X:jax.Array, t:float) -> jax.Array:
            Calculates the right-hand side of the ODE.
        Args:
            X:jax.Array containing the generalized coordinates/coordinate
            followed by their velocities/its velocity.
            E.g. jnp.array([q, q_dot]).
            t:float The time variable.
            Might be used in case system is time-dependent.
        Returns:
            The right-hand side of the ODE,
            a jax.Array of shape n_coordinates * 2.
        rhs may use jnp syntax in the form "jnp.sin(...)".
Returns:
  save_message:str A message that the prediction has been saved.

```

2. Single particles in 2d

This section contains the description of the system and tools provided to the agent for the 2d systems with a single particle (damped Mexican hat potential, particle in off-center gravity, arbitrary 2d potential).

Description supplied to agent for the 2d systems with a single particle

This is single physical system moving in two spatial dimensions with the coordinates:
 q0: the real space x-coordinate of the moving particle,
 [...]

The experiment tools and the tool to save the result are equivalent to Supplement S 4 A 1.

3. Multiple particles in 2d

This section contains the description of the system and tools provided to the agent for the 2d systems with multiple particles (two particles with gravity, three particles with gravity, ten particles with exponential potential).

Description supplied to agent for the 2d systems with multiple particles

This is a physical system governed by an ordinary differential equation. The system consists of <N> particles moving in two dimensions.

Here, <N> is replaced with the appropriate number depending on the system.

For the systems with two and three particles with gravity, we use the following experiment tools (slightly adapted depending on the number of particles):

Experiment: observe evolution given initial conditions (two and three particles with gravity)

```

def observe_evolution(x1: float, y1: float, x2:float, y2:float, vx1 :float, vy1:float, vx2:
float, vy2:float):
  Observe a trajectory of the system given initial conditions.
  A reasonable coordinate range is e.g. (-1., 1.).
  Args:
    x1: first particle's initial x-coordinate
    [...]
  Returns:
    'ts':jax.Array of shape [nsteps] with the time steps

```

```
'array':jax.Array of shape [nsteps,dimension] with the solution,
      array[:, 0] holds the first particle's x-coordinate
      [...]
```

For the system with ten particles with an exponential potential, we use slightly adapted experiment tools to accommodate the large number of coordinates:

Experiment: observe evolution given initial conditions (ten particles with exponential potential)

```
observe_evolution(x_list: str, y_list: str, vx_list: str, vy_list: str)
  Observe a trajectory of the system given initial conditions.
  A reasonable coordinate range is e.g. [-3., 3.].
  Args:
    x1_list: list of initial x-positions in the form '[value1, value2, ...]'
    [...]
  Returns:
    'ts':jax.Array of shape [nsteps] with the time steps
    'array':jax.Array of shape [nsteps, 4 * N_particles] with the solution,
      array[:, 0] holds the first particle x-position
      array[:, 1] holds the first particle y-position
      ...
      array[:, 2 * N_particles] holds the first particle x-velocity
      array[:, 2 * N_particles + 1] holds the first particle y-velocity
      ...
```

The tool to save the result is the same as in Supplement S4 A 1.

4. Systems with hidden degrees of freedom

Description supplied to agent for oscillators with hidden degrees of freedom

This is a physical system governed by an ordinary differential equation. This system consists of multiple particles moving in one dimension. However, you can only observe the position and velocity of the first particle. The initial positions and velocities of the hidden particles are the same for each observed evolution.

Default description supplied to agent for particles in gravity with hidden degrees of freedom

This is a physical system governed by an ordinary differential equation. This system consists of multiple particles in 2D. Only the first particle (x,y,vx,vy) is observed; the rest are hidden.

The experiment tools are the same as in Supplement S4 A 1. To save the result, we use (with slight modifications for particles in gravity to accommodate the different number of dimensions):

Save predicted equation of motion for oscillators with hidden degrees of freedom

```
save_result_find_eom_hidden_degrees(rhs: str, hidden_initial_qs:str, hidden_initial_q_dots:
str):
  Compare the provided right-hand side of the ordinary differential equation with the
  true right-hand side governing the differential equation of the system.
  The loss is computed as the mean squared error between the true rhs and predicted rhs
  at some randomly sampled points.
  This tool should only be used to provide the final result.
  It can only be called once per experiment.
  Args:
    rhs: Define the right-hand side of an ordinary differential equation.
    You pass a python code that must be of the form
      def rhs(X:jax.Array, t:float) -> jax.Array:
```

Damped Duffing oscillator $\ddot{x} = -ax^3 - bx - \gamma\dot{x}$	reasonable coordinate range $[-1, 1]$ $a = 4.528, b = 1.625, \gamma = 0.043$
Damped pendulum $\ddot{x} = -\alpha \sin(x) - \gamma\dot{x}$	reasonable coordinate range $[-3, 3]$ $\alpha = 1.712, \gamma = 0.043$
Damped asymmetric double well $\ddot{x} = -ax^3 + bx + c - \gamma\dot{x}$	reasonable coordinate range $[-1, 1]$ $a = 4.528, b = 1.625, c = 0.1, \gamma = 0.043$
Velocity position coupling $\ddot{x} = -ax^2\dot{x} - kx$	reasonable coordinate range $[-1, 1]$ $a = 1.7, k = 0.4,$
Arbitrary 1d potential $\ddot{x} = -x - a \cos(kx)$	reasonable coordinate range $[-3, 3]$ $a = 4.8, k = 6$
Damped driven oscillator $\ddot{x} = -kx - \gamma\dot{x} + A \cos(\omega t)$	reasonable coordinate range $[-1, 1]$ $k = 2.319, \gamma = 0.6, A = 1.712, \omega = 1.551$
Damped parametric oscillator $\ddot{x} = -(k + A \cos(\omega t))x - \gamma\dot{x}$	reasonable coordinate range $[-1, 1]$ $k = 2.319, A = 1.712, \omega = 1.551, \gamma = 0.3$
Damped double pendulum $\Delta = \theta_1 - \theta_2$ $\ddot{\theta}_1 = -\frac{(2m_1+m_2)\sin(\theta_1)-m_2\sin(\theta_1-2\theta_2)-2\sin(\Delta)m_2(\omega_2^2 l_2+\omega_1^2 l_1 \cos(\Delta))}{l_1(2m_1+m_2-m_2 \cos(2\Delta))} - \gamma\dot{\theta}_1$ $\ddot{\theta}_2 = \frac{2\sin(\Delta)(\omega_1^2 l_1(m_1+m_2)+(m_1+m_2)\cos(\theta_1)+\omega_2^2 l_2 m_2 \cos(\Delta))}{l_2(2m_1+m_2-m_2 \cos(2\Delta))} - \gamma\dot{\theta}_2$	reasonable coordinate range $[-3, 3]$ $m_1 = m_2 = 1$ $l_1 = 1.712, l_2 = 0.851$ $\gamma = 0.143$
Two damped coupled oscillators $\ddot{x}_1 = -k_1 x_1 + k_{12}(x_2 - x_1) - \gamma\dot{x}_1$ $\ddot{x}_2 = -k_2 x_2 - k_{12}(x_2 - x_1) - \gamma\dot{x}_2$	reasonable coordinate range $[-1, 1]$ $k_1 = 1.712, k_{12} = 0.15$ $\gamma = 0.043$
Three damped coupled oscillators Analogous to two coupled oscillators, $k_1 = 1, k_2 = 1.5, k_3 = 0.5, k_{1,2} = 0.2, k_{13} = 0.3, k_{23} = 0.4$	reasonable coordinate range $[-1, 1]$
Damped Mexican hat potential $\ddot{x} = (a - b(x^2 + y^2))x - \gamma\dot{x}$ $\ddot{y} = (a - b(x^2 + y^2))y - \gamma\dot{y}$	reasonable coordinate range $[-1, 1]$ $a = 4, b = 2.8$ $\gamma = 0.2$
Particle in off-center gravity $r = \sqrt{(x - c_x)^2 + (y - c_y)^2}$ $\ddot{x} = -\frac{G(x-c_x)}{r^3}, \ddot{y} = -\frac{G(y-c_y)}{r^3}$	reasonable coordinate range $[-2, 2]$ $c_x = -0.7, c_y = 0.2$ $G = 2.3$
Arbitrary 2d potential $r = \sqrt{(x^2 + y^2)}$ $\ddot{x} = -kx - \frac{ax \cos(6r)}{r}, \ddot{y} = -ky - \frac{ay \cos(6r)}{r}$	reasonable coordinate range $[-2, 2]$ $k = 0.6$ $a = 0.8$
Two particles with gravity $\Delta_x = x_1 - x_2, \Delta_y = y_1 - y_2, r = \sqrt{\Delta_x^2 + \Delta_y^2}$ $\ddot{x}_1 = -\frac{m_2 \Delta_x}{r^3}, \ddot{y}_1 = -\frac{m_2 \Delta_y}{r^3}, \ddot{x}_2 = \frac{m_1 \Delta_x}{r^3}, \ddot{y}_2 = \frac{m_1 \Delta_y}{r^3}$	reasonable coordinate range $[-1, 1]$ $m_1 = 8.123$ $m_2 = 0.781$
Three particles with gravity Analogous to two particles in gravity, $m_1 = 1.3, m_2 = 9.0, m_3 = 0.2$	reasonable coordinate range $[-2, 2]$
Ten particles with exponential potential $r_{ij} = \sqrt{(x_i - x_j)^2 + (y_i - y_j)^2}$ $\ddot{x}_i = \sum_j -ab \frac{x_i - x_j}{r_{ij}} \exp(-br_{ij}), \ddot{y}_i = \sum_j -ab \frac{y_i - y_j}{r_{ij}} \exp(-br_{ij})$	$a = 0.8$ $b = 1.3$
Two partially observed oscillators Analogous to two coupled oscillators, $k_1 = 1.1, k_2 = 1.54, k_{12} = 1.2, \gamma = 0$ Hidden initial conditions, $x_2 = 0.4, \dot{x}_2 = -0.2$	reasonable coordinate range $[-2, 2]$
Three partially observed oscillators Analogous to three coupled oscillators, $k_1 = 0.611, k_2 = 1.907, k_3 = 1.473, k_{12} = 1.317, k_{13} = 0.537, k_{23} = 1.811, \gamma = 0$ Hidden initial conditions, $x_2 = -0.123, \dot{x}_2 = 0.895, x_3 = 0.068, \dot{x}_3 = 0.957$	reasonable coordinate range $[-2, 2]$
Two partially observed particles with gravity Analogous to two particles in gravity, $m_1 = 0.7, m_2 = 1.8$ Hidden initial conditions, $x_2 = 0.5, y_2 = 0.5, \dot{x}_2 = -0.5, \dot{y}_2 = 0$	reasonable coordinate range $[-3, 3]$

TABLE S1. Equations of motion for the considered mechanical systems.

```

Calculates the right-hand side of the ODE.
Make sure to also include the hidden dimensions in X.
X is of shape (n_visible + n_hidden) * 2 where the first half
contains the coordinates and the second half contains the velocities.
E.g. for 1 visible and 1 hidden dimension, X is of shape (2*2,) and
of the form jnp.array([q0, q1, q0_dot, q1_dot]),
where q0 and q0_dot are the observed quantities.
Make sure to adhere to this format.
Args:
  X:jax.Array containing the generalized coordinates (including the
    hidden coordinates) followed by their velocities.
    E.g. jnp.array([q0, q1, q0_dot, q1_dot]).
  t:float The time variable. Might be used in case system is
    time-dependent.
Returns:
  The right-hand side of the ODE,
  a jnp.array of shape n_coordinates * 2.
  rhs may use jnp syntax in the form "jnp.sin(...)".
  rhs must be jax-jittable!
hidden_initial_qs: A string representation of a list of initial values for the
hidden (not the observed!) generalized coordinates,
e.g. '[0.1, ...]' with length n_hidden.
hidden_initial_q_dots: A string representation of a list of initial values for
the hidden (not the observed!) generalized velocities,
e.g. '[0.0, ...]' with length n_hidden.
Returns:
  save_message:str A message that the prediction has been saved.

```

B. Wave systems

The agent is tasked to find the governing equation of a complex-valued field on a 1d tight-binding lattice. Additionally, it is given the number of lattice points, the maximum experiment time, and the space and time resolution of the system. We show the dynamics of the considered fields in Figure S3 and the exact equations of motion in Table S2.

Default description supplied to agent in field tasks

This is a mystery system, showing the evolution of a complex-valued field evolving on a 1D tight-binding lattice of 100 lattice points, with periodic boundary conditions. The x grid runs from -5 to 5. For observational experiments, time runs up to 20 with 200 time grid points.

The agent can run an experiment via the following tool:

Experiment: observe the evolution of a field with given initial conditions

```

def run_field_evolution_experiment(initial_condition_code:str):
  Run one experiment of the evolution of the mystery field,
  where you can choose the initial condition.
  Args:
    initial_condition_code: python code with
      jax syntax that set the variable phi0,
      which represents the complex
      field at time 0.
      Use jnp.sin(...) etc, and use the
      array x which represents the position
      coordinate on a 1D grid.
  Returns:
    Solution with entries
    - ts: the time points (1D array)
    - x: the x grid (1D array)
    - phis: the complex field solution,
      a 2D jax.Array of shape [n_ts,n_x]

```

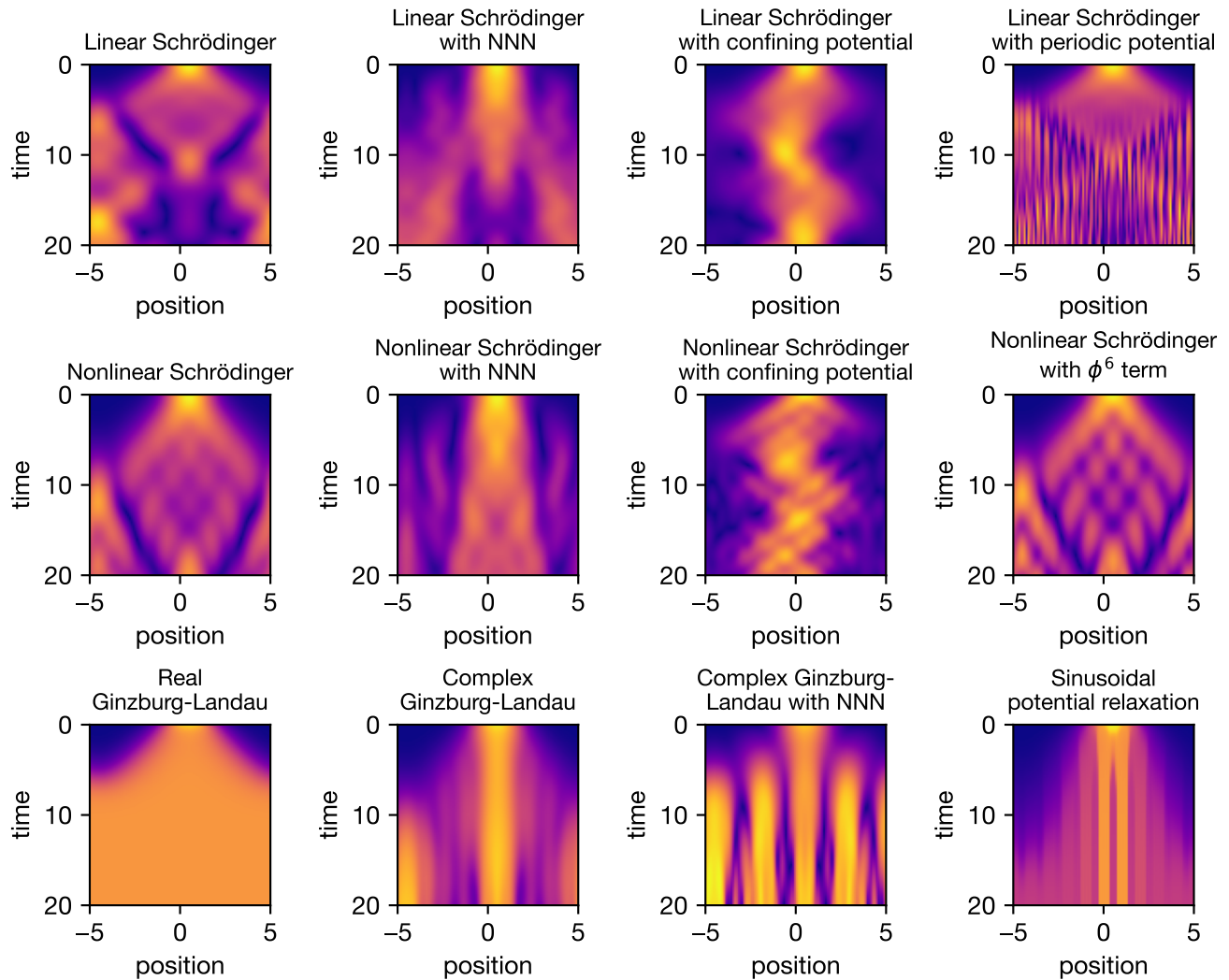


FIG. S3. **Field dynamics.** Dynamics of the different field systems with a Gaussian wave packet as the initial condition. The squared absolute value of the field $|\phi|^2$ is depicted with the color scale ranging from blue (zero) to yellow (high).

The agent saves its result via:

Save prediction for field systems

```
def save_result_find_eom(code:str):
    Save the result of your analysis, providing the code that would define the equations of
    motion of the field. You pass a python code that must be of the form:
    Define the right-hand side of a complex field equation to be simulated.
    The field equation will be simulated using the split-step method, applying potential
    terms in real space and kinetic terms (from spatial derivatives) in Fourier space.
    You pass a python code that must be of the form:

    def U_potential(phi,x,t,dt):
        # jax code that calculates the evolution of the
        # complex field phi for a time step dt at time t
        # and returns the result. This evolution here
        # only accounts for the terms of the field partial differential equation
        # that do not involve spatial derivatives (those
        # will be handled separately). x is a 1D array for
        # the real-space grid points.
```

Linear Schrödinger	$i \frac{d\phi_n}{dt} = -\frac{1}{2}(\Delta_d\phi)_n$
$U_{\text{kin}}(\phi_k, k, t, \Delta t) = \exp(-i[1 - \cos(k)]\Delta t) \phi_k$ $U_{\text{pot}}(\phi, x, t, \Delta t) = \phi$	
Linear Schrödinger with NNN	$i \frac{d\phi_n}{dt} = (A - 1 + B)\phi_n - \frac{1}{2}(\Delta_d\phi)_n + \frac{B}{2}(\Delta_{d,2}\phi)_n$ $A = 0.5, B = 0.5$
$U_{\text{kin}}(\phi_k, k, t, \Delta t) = \exp(-i[A - \cos(k) + B \cos(2k)]\Delta t) \phi_k$ $U_{\text{pot}}(\phi, x, t, \Delta t) = \phi$	
Linear Schrödinger with confining potential	$i \frac{d\phi_n}{dt} = -\frac{1}{2}(\Delta_d\phi)_n + B \cos\left(\frac{\pi x_n}{x_{\text{max}}}\right)\phi_n$ $B = -0.5, x_{\text{max}} = 5$
$U_{\text{kin}}(\phi_k, k, t, \Delta t) = \exp(-i[1 - \cos(k)]\Delta t) \phi_k$ $U_{\text{pot}}(\phi, x, t, \Delta t) = \exp(-iB \cos(\pi x/x_{\text{max}})\Delta t) \phi$	
Linear Schrödinger with periodic potential	$i \frac{d\phi_n}{dt} = -\frac{1}{2}(\Delta_d\phi)_n + B \cos\left(\frac{2\pi N x_n}{x_{\text{max}}}\right)\phi_n$ $B = 0.2, N = 10, x_{\text{max}} = 5$
$U_{\text{kin}}(\phi_k, k, t, \Delta t) = \exp(-i[1 - \cos(k)]\Delta t) \phi_k$ $U_{\text{pot}}(\phi, x, t, \Delta t) = \exp(-iB \cos(2\pi N x/x_{\text{max}})\Delta t) \phi$	
Nonlinear Schrödinger	$i \frac{d\phi_n}{dt} = -\frac{A}{2}(\Delta_d\phi)_n + B \phi_n ^2\phi_n$ $A = 0.5$ $B = 0.25$
$U_{\text{kin}}(\phi_k, k, t, \Delta t) = \exp(-iA[1 - \cos(k)]\Delta t) \phi_k$ $U_{\text{pot}}(\phi, x, t, \Delta t) = \exp(-iB \phi ^2\Delta t) \phi$	
Nonlinear Schrödinger with NNN	$i \frac{d\phi_n}{dt} = (AB - 1 + AC)\phi_n - \frac{A}{2}(\Delta_d\phi)_n$ $+ \frac{AC}{2}(\Delta_{d,2}\phi)_n + D \phi_n ^2\phi_n$ $A = 0.5, B = 1.5, C = 0.5$ $D = 0.25$
$U_{\text{kin}}(\phi_k, k, t, \Delta t) = \exp(-i[A(B - \cos(k) + C \cos(2k))]\Delta t) \phi_k$ $U_{\text{pot}}(\phi, x, t, \Delta t) = \exp(-iD \phi ^2\Delta t) \phi$	
Nonlinear Schrödinger with confining potential	$i \frac{d\phi_n}{dt} = -\frac{1}{2}(\Delta_d\phi)_n + \left(-\cos\left(\frac{\pi x_n}{x_{\text{max}}}\right) + \phi_n ^2\right)\phi_n$ $N = 10, x_{\text{max}} = 5$
$U_{\text{kin}}(\phi_k, k, t, \Delta t) = \exp(-i[1 - \cos(k)]\Delta t) \phi_k$ $U_{\text{pot}}(\phi, x, t, \Delta t) = \exp(-i[-\cos(\pi x/x_{\text{max}}) + \phi ^2]\Delta t) \phi$	
Nonlinear Schrödinger with ϕ^6 term	$i \frac{d\phi_n}{dt} = -\frac{A}{2}(\Delta_d\phi)_n + B(\phi_n ^2 + 2 \phi_n ^4)\phi_n$ $A = 0.5$ $B = 0.25$
$U_{\text{kin}}(\phi_k, k, t, \Delta t) = \exp(-iA[1 - \cos(k)]\Delta t) \phi_k$ $U_{\text{pot}}(\phi, x, t, \Delta t) = \exp(-iB(\phi ^2 + 2 \phi ^4)\Delta t) \phi$	
Real Ginzburg–Landau	$\frac{d\phi_n}{dt} = -A(\Delta_d\phi)_n - B(2 \phi_n ^2 - 1)\phi_n$ $A = 0.5$ $B = 0.5$
$U_{\text{kin}}(\phi_k, k, t, \Delta t) = \exp(-A[1 - \cos(k)]\Delta t) \phi_k$ $U_{\text{pot}}(\phi, x, t, \Delta t) = \exp(-B(2 \phi ^2 - 1)\Delta t) \phi$	
Complex Ginzburg–Landau	$\frac{d\phi_n}{dt} = -A(\Delta_d\phi)_n - B(2C \phi_n ^2 - 1)\phi_n$ $A = 0.2(0.5 + 2i)$ $B = 0.2, C = (1 - 1.5i)$
$U_{\text{kin}}(\phi_k, k, t, \Delta t) = \exp(-A[1 - \cos(k)]\Delta t) \phi_k$ $U_{\text{pot}}(\phi, x, t, \Delta t) = \exp(-B(2C \phi ^2 - 1)\Delta t) \phi$	
Complex Ginzburg–Landau with NNN	$\frac{d\phi_n}{dt} = -A\left[(B - 1 + C)\phi_n - \frac{1}{2}(\Delta_d\phi)_n + \frac{C}{2}(\Delta_{d,2}\phi)_n\right]$ $- D(2E \phi_n ^2 - 1)\phi_n$ $A = 0.8(0.5 + 0.5i), B = 0.65, C = 0.8$ $D = 0.2, E = (1 - 1.5i)$
$U_{\text{kin}}(\phi_k, k, t, \Delta t) = \exp(-A[B - \cos(k) + C \cos(2k)]\Delta t) \phi_k$ $U_{\text{pot}}(\phi, x, t, \Delta t) = \exp(-D(2E \phi ^2 - 1)\Delta t) \phi$	
Sinusoidal potential relaxation	$\frac{d\phi_n}{dt} = -A(\Delta_d\phi)_n + B \sin(C \phi_n ^2)\phi_n$ $A = 0.5$ $B = 0.1, C = 15$
$U_{\text{kin}}(\phi_k, k, t, \Delta t) = \exp(-A[1 - \cos(k)]\Delta t) \phi_k$ $U_{\text{pot}}(\phi, x, t, \Delta t) = \exp(B \sin(C \phi ^2)\Delta t) \phi$	

TABLE S2. Field equation and corresponding kinetic and potential propagators for field systems. Here $(\Delta_d\phi)_n = \phi_{n+1} - 2\phi_n + \phi_{n-1}$ and $(\Delta_{d,2}\phi)_n = \phi_{n+2} - 2\phi_n + \phi_{n-2}$.

```
# Example: return jnp.exp(-1j*dt*0.1*jnp.sin(x))*phi
def U_kinetic(phi_k,k,t,dt):
# jax code that calculates the evolution of phi_k
```

```

    # from the spatial-derivative terms in the field equation,
    # for a time step dt at time t and returns the result.
    # phi_k is the field in Fourier space. k is a 1D array
    # for the Fourier space grid points.
    # Example: return jnp.exp(-1j*(1-jnp.cos(k))*dt)*phi_k
Use jax.numpy syntax in the form "jnp.exp(...)".

Args:
    code: The code.
Returns:
    'save_message' A message that the prediction has been saved.

```

C. Quantum systems

The agent is asked to discover the underlying Hamiltonian for an unknown quantum many-body system composed of spins (spin 1/2, i.e. qubits). In some cases, the Hamiltonian may contain one or several parameters (fields, couplings). In some cases, the agent can change the size N of the experimental system as well. The agent does not have any information except that it is dealing with a spin 1/2 system and that the number of spins is a certain value (or variable). If there is a parameter, the agent is just being told the name of that parameter (e.g. 'A') without reference to its meaning. The exact Hamiltonians are specified in Table S3.

The system is described in the following way:

Default description supplied to agent in quantum tasks

You do have access to an experimental system of ... spins.

Description in case of variable system size

You do have access to an experimental system of N spins, where you can select the number N (size of the system).

Additional description for partially observed dynamics

You will only be able to observe the spins ...list of spin indices... of this system, whose spin expectation values will be returned in this order.

Further text for restricted control

You will only be able to control the $N_{\text{control}}=...$ spins that are also observable. All others will be set to some fixed default values every time you start an experiment.

Variable parameters (example)

The system has one tunable parameter A that you must set. [analogously for two parameters]

To save its prediction, the agent uses:

Save prediction for quantum systems

```

def announce_Hamiltonian(Hamiltonian: str):
    Announce the correct Hamiltonian, in the form of python code.
    You pass a python code that must produce an operator H, constructing it out of provided
    spin operators. Here Sx is a list of spin operator x-components, Sy likewise for the y-
    components, and Sz for the z-components. These are Pauli matrices.
    They can be accessed like Sx[2] etc. Remember to use the "@" matrix multiplication

```

GS Transverse-field Ising chain	
$\hat{H} = J \sum_{j=0}^{N-2} \hat{\sigma}_j^z \hat{\sigma}_{j+1}^z - h \sum_{j=0}^{N-1} \hat{\sigma}_j^x$	$N = 10, J = 1.5, h = 0.6$
GS Transverse-field Ising chain with tunable coupling	
$\hat{H} = A \sum_{j=0}^{N-2} \hat{\sigma}_j^z \hat{\sigma}_{j+1}^z - h \sum_{j=0}^{N-1} \hat{\sigma}_j^x$	$N = 10, h = 0.6, A$ tunable
GS Transverse-field Ising chain with tunable coupling and number of spins	
$\hat{H} = A \sum_{j=0}^{N-2} \hat{\sigma}_j^z \hat{\sigma}_{j+1}^z - h \sum_{j=0}^{N-1} \hat{\sigma}_j^x$	N tunable, $h = 0.6, A$ tunable,
GS 2d Heisenberg model	
$\hat{H} = J \sum_{\langle r, r' \rangle} (\hat{\sigma}_r^x \hat{\sigma}_{r'}^x + \hat{\sigma}_r^y \hat{\sigma}_{r'}^y + \hat{\sigma}_r^z \hat{\sigma}_{r'}^z) - h \sum_r \hat{\sigma}_r^x$	$N = 9, J = 1, h = 2$
GS 2d Heisenberg model with tunable coupling	
$\hat{H} = 2A \sum_{\langle r, r' \rangle} (\hat{\sigma}_r^x \hat{\sigma}_{r'}^x + \hat{\sigma}_r^y \hat{\sigma}_{r'}^y + \hat{\sigma}_r^z \hat{\sigma}_{r'}^z) - h \sum_r \hat{\sigma}_r^x$	$N = 9, h = 2, A$ tunable
GS 2d Heisenberg model with tunable coupling and field strength	
$\hat{H} = 2A \sum_{\langle r, r' \rangle} (\hat{\sigma}_r^x \hat{\sigma}_{r'}^x + \hat{\sigma}_r^y \hat{\sigma}_{r'}^y + \hat{\sigma}_r^z \hat{\sigma}_{r'}^z) - 2B \sum_r \hat{\sigma}_r^x$	$N = 9, A$ tunable, B tunable
GS Topological Ising chain	
$\hat{H} = K \sum_{j=0}^{N-3} \hat{\sigma}_j^z \hat{\sigma}_{j+1}^x \hat{\sigma}_{j+2}^z - J \sum_{j=0}^{N-2} \hat{\sigma}_j^z \hat{\sigma}_{j+1}^z - h \sum_{j=0}^{N-1} \hat{\sigma}_j^x$	$N = 10, K = 0.5, J = 1, h = 0.3$
GS Topological Ising chain with tunable coupling	
$\hat{H} = A \sum_{j=0}^{N-3} \hat{\sigma}_j^z \hat{\sigma}_{j+1}^x \hat{\sigma}_{j+2}^z - J \sum_{j=0}^{N-2} \hat{\sigma}_j^z \hat{\sigma}_{j+1}^z - h \sum_{j=0}^{N-1} \hat{\sigma}_j^x$	$N = 10, A$ tunable, $J = 1, h = 1$
GS Topological Ising chain with tunable coupling and number of spins	
$\hat{H} = A \sum_{j=0}^{N-3} \hat{\sigma}_j^z \hat{\sigma}_{j+1}^x \hat{\sigma}_{j+2}^z - J \sum_{j=0}^{N-2} \hat{\sigma}_j^z \hat{\sigma}_{j+1}^z - h \sum_{j=0}^{N-1} \hat{\sigma}_j^x$	N tunable, A tunable, $J = 1, h = 1$
GS Arbitrary Hamiltonian	
$\hat{H} = J_{xz} \sum_{j=0}^{N-2} \hat{\sigma}_j^x \hat{\sigma}_{j+1}^z - J_{yx} \sum_{j=0}^{N-2} \hat{\sigma}_j^y \hat{\sigma}_{j+1}^x - h_x \sum_{j=0}^{N-1} \hat{\sigma}_j^x + h_y \sum_{j=0}^{N-1} \hat{\sigma}_j^y$	$N = 10, J_{xz} = 1.5, J_{yx} = 0.7, h_x = 0.6, h_y = 0.4$
DYN Arbitrary Hamiltonian	
$\hat{H} = J_1 \hat{\sigma}_0^x \hat{\sigma}_1^z + J_2 \hat{\sigma}_0^y \hat{\sigma}_2^x - h_1 \hat{\sigma}_1^y + h_2 \hat{\sigma}_2^y - K \hat{\sigma}_1^x \hat{\sigma}_2^y$	$N = 3, J_1 = 1, J_2 = 0.5, h_1 = 0.7, h_2 = 0.3, K = 0.8$
DYN Arbitrary Hamiltonian with access to two spins	
$\hat{H} = J_1 \hat{\sigma}_0^x \hat{\sigma}_1^z + J_2 \hat{\sigma}_0^y \hat{\sigma}_2^x - h_1 \hat{\sigma}_1^y + h_2 \hat{\sigma}_2^y - K \hat{\sigma}_1^x \hat{\sigma}_2^y$	$N = 3, J_1 = 1, J_2 = 0.5, h_1 = 0.7, h_2 = 0.3, K = 0.8$
DYN Arbitrary Hamiltonian with access to two spins with tunable field	
$\hat{H} = J_1 \hat{\sigma}_0^x \hat{\sigma}_1^z + J_2 \hat{\sigma}_0^y \hat{\sigma}_2^x - A \hat{\sigma}_1^y + h_2 \hat{\sigma}_2^y - K \hat{\sigma}_1^x \hat{\sigma}_2^y$	$N = 3, J_1 = 1, J_2 = 0.5, h_2 = 0.3, K = 0.8, A$ tunable
DYN Heisenberg chain	
$\hat{H} = J \sum_{j=0}^{N-2} (\hat{\sigma}_j^x \hat{\sigma}_{j+1}^x + \hat{\sigma}_j^y \hat{\sigma}_{j+1}^y + \hat{\sigma}_j^z \hat{\sigma}_{j+1}^z) - h \sum_{j=0}^{N-1} \hat{\sigma}_j^x$	$N = 10, J = 0.5, h = 1.5$
DYN Heisenberg chain with tunable field	
$\hat{H} = J \sum_{j=0}^{N-2} (\hat{\sigma}_j^x \hat{\sigma}_{j+1}^x + \hat{\sigma}_j^y \hat{\sigma}_{j+1}^y + \hat{\sigma}_j^z \hat{\sigma}_{j+1}^z) - A \sum_{j=0}^{N-1} \hat{\sigma}_j^x$	$N = 10, J = 0.5, A$ tunable
DYN Heisenberg chain with access to two spins with tunable field	
$\hat{H} = J \sum_{j=0}^{N-2} (\hat{\sigma}_j^x \hat{\sigma}_{j+1}^x + \hat{\sigma}_j^y \hat{\sigma}_{j+1}^y + \hat{\sigma}_j^z \hat{\sigma}_{j+1}^z) - A \sum_{j=0}^{N-1} \hat{\sigma}_j^x$	$N = 10, J = 0.5, A$ tunable
DYN Transverse-field Ising chain with tunable coupling	
$\hat{H} = A \sum_{j=0}^{N-2} \hat{\sigma}_j^z \hat{\sigma}_{j+1}^z - h \sum_{j=0}^{N-1} \hat{\sigma}_j^x$	$N = 10, A$ tunable, $h = 1$
DYN Transverse-field Ising chain with access to two spins with tunable coupling	
$\hat{H} = A \sum_{j=0}^{N-2} \hat{\sigma}_j^z \hat{\sigma}_{j+1}^z - h \sum_{j=0}^{N-1} \hat{\sigma}_j^x$	$N = 10, A$ tunable, $h = 1$

TABLE S3. Hamiltonians for the considered quantum ground state (GS) and dynamics tasks (DYN).

operator when taking the product of several spin operators.
 If the Hamiltonian contains a tunable parameter (or several), use the parameter name(s) specified in the problem description and do not substitute numerical values. However, if the Hamiltonian contains non-tunable numerical parameters, specify them as floating point numbers.

Returns:

Message that the Hamiltonian has been stored.

1. Ground state tasks

For ground state tasks, the agent has access to the following experiment tools:

Experiment: define operators to be observed in ground state of system

```
set_operator_for_ground_state(operator_label: str, operator_code: str)
Define a Hermitian operator, whose expectation value in the ground state of
the experimental system can later be evaluated.
You pass a python code that must produce an operator H, constructing
it out of provided spin operators. Here Sx is a list of spin operator x-components,
Sy likewise for the y-components, and Sz for the z-components.
These are Pauli matrices.
They can be accessed like Sx[2] etc. Remember to use
the "@" matrix multiplication operator when taking
the product of several spin operators.
Otherwise you can use jax.numpy syntax in the form "jnp.sin(...)".
Args:
  operator_label: the label the operator will be stored under.
  operator_code: the python code defining the operator.
Returns:
  Message indicating wether the operator was set successfully.
```

Experiment: observe expectation values in ground state with variable physical parameter

```
run_experiment_ground_state_with_parameters(set_params_code: str, operators: str)
Measure the ground state expectation values for several operators, for the given
experimental system, for given physical parameters. If the experimental system
has variable size N, you must also set N in the code given here!
Args:
  set_params_code: python code that sets the numerical values of the system
  parameters.
  operators: a string with a comma-delimited list of operator labels (previously
  defined via set_operator)
Returns:
  dict containing the expectation values for each of the operators (dict key named
  according to the operator label)
```

In experiments without tunable parameters, the preceding tool is replaced by an equivalent tool with the parts related to setting the parameters removed.

2. Dynamics tasks

For dynamics tasks, the agent has access to the following experiment tool (again, slightly adapted if the system has no tunable parameters):

Experiment: observe dynamics with variable physical parameter

```
def run_experiment_with_parameters(bloch_vectors:jax.Array, T: float, dt: float,
    parameter_code: str):
    Run an experiment on the spin system. You can provide the normalized Bloch
    vectors to describe the initial product state. The system will evolve
    according to its time-independent Hamiltonian, and the evolution of the
    spin expectation values will be returned. The spins are described
    by Pauli operators Sx, Sy, and Sz. The number N_obs of observable spin
    operators may be smaller than the total number N of spins. The number N_control
    of controllable spin operators may be smaller than the total number N (see
    description of experimental setup).
    Args:
        bloch_vectors: array (jax.Array) of shape (N_control,3) of Bloch vectors.
        T: total time duration of experiment.
        dt: time step between observations. nsteps will be int(T/dt)+1.
        parameter_code: python code that sets the parameter numerical values
    Returns:
        'ts': jax.Array of shape [nsteps] (with the time steps 'nsteps')
        'Sx_t': jax.Array of shape [N_obs,nsteps] with the expectation values of all
        observed Sx operators
        'Sy_t': jax.Array of shape [N_obs,nsteps] with the expectation values of all
        observed Sy operators
        'Sz_t': jax.Array of shape [N_obs,nsteps] with the expectation values of all
        observed Sz operators
```

In Table S3, we list all the Hamiltonians for the test scenarios considered in the main text ("GS" marks ground state tasks, "DYN" dynamical tasks).

S5. EXAMPLE CONVERSATIONS

To give an impression of typical strategies used by the agent, we ask GPT 5 pro to summarize example conversations. The LLM is asked to produce LaTeX code and to include the original visualizations that the SciExplorer generated (in their original resolution). We show the discovery of the equations of motion of a particle in an asymmetric double well potential with damping in Supplement S5A, the discovery of the equations of motion of three coupled harmonic oscillators, where only one can be observed in Supplement S5B, a failed exploration of the arbitrary 2d potential system in Supplement S5C, the discovery of a complex Ginzburg-Landau equation with next-nearest-neighbor interactions in Supplement S5D, the discovery of a transverse field Ising model with tunable coupling from ground state expectation values in Supplement S5E, and the discovery of a Heisenberg Hamiltonian by observing dynamics in Supplement S5F.

A. Asymmetric double well

The following text is entirely LLM-generated.

Goal of the conversation

The goal was to infer the equations of motion (EOM) of an unknown physical system known to be governed by an ordinary differential equation, and to determine both its qualitative form (model structure) and numerical parameters. The solution had to be obtained purely from trajectories generated by the system under a wide range of initial conditions, and validated by forward simulation and statistical diagnostics.

Overview of approach

I pursued a model-based system identification program: (i) enumerate physically plausible hypotheses for the EOM, (ii) generate diverse trajectory data, (iii) visualize the dynamics, (iv) estimate accelerations and regress candidate right-hand sides, (v) analyze residuals to refine the model class, (vi) re-simulate with the inferred EOM and compare against data, (vii) extract physical implications (potential landscape, equilibria, small-oscillation frequencies), and (viii) finalize the EOM with parameter uncertainties.

Candidate hypotheses

To span common second-order autonomous oscillators, I considered: harmonic (undamped/damped), driven harmonic, conservative and damped Duffing (single or double well), pendulum (with damping), van der Pol and Rayleigh self-excited oscillators, linear and quadratic drag, Coulomb friction, parametric (Mathieu), and generic mixed nonlinearities such as cubic-quintic forces and nonlinear damping of the form $(\gamma_0 + \gamma_2 q^2)\dot{q}$. This catalog guided the subsequent elimination process.

Data generation and first diagnostics

I ran two 5-trajectory batches covering extreme and moderate initial states: Batch A varied position with zero velocity, $q_0 \in \{-1, -0.5, 0, 0.5, 1\}$, $\dot{q}_0 = 0$; Batch B fixed $q_0 = 0$ and varied velocity $\dot{q}_0 \in \{-1, -0.5, 0, 0.5, 1\}$. Figure S4 shows the resulting time series and phase portraits.

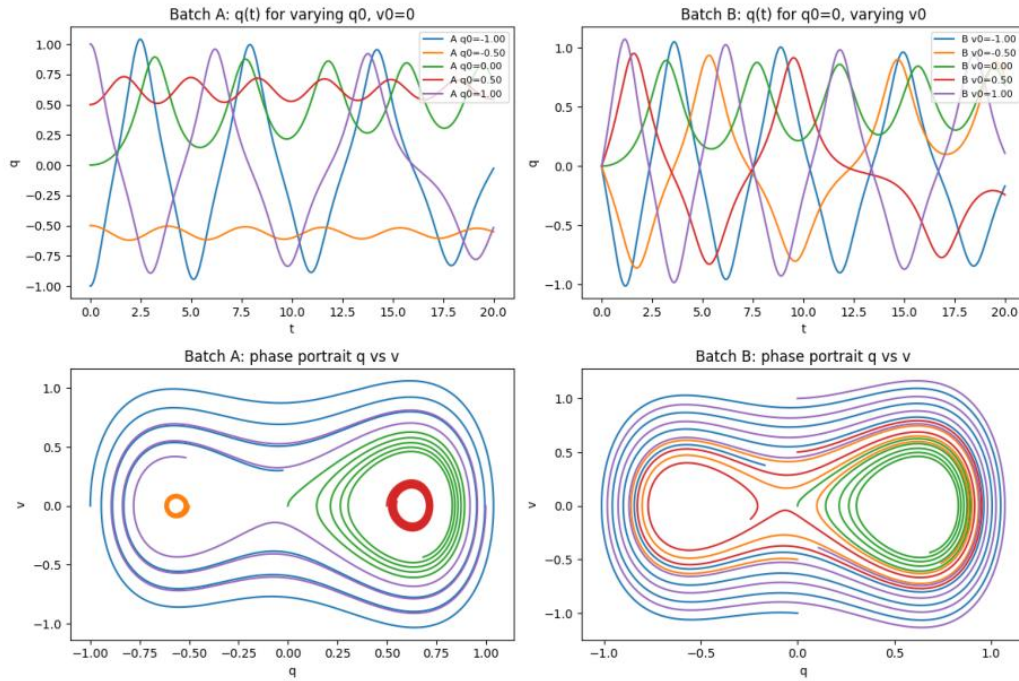


FIG. S4. Initial exploration. Top row: representative $q(t)$ for Batches A and B. Bottom row: phase portraits. Two lobes with slow spirals indicate a double-well potential with weak damping; slight left-right asymmetry suggests a constant bias.

What we learned: - The phase portraits are two-lobed with slow inward spirals, consistent with a double-well Duffing-like potential and linear damping; this ruled out single-well harmonic motion and self-excited limit cycles (van der Pol/Rayleigh). - The left-right asymmetry hinted at a constant bias force, incompatible with a strictly odd conservative force.

Still plausible hypotheses: - Damped Duffing with or without a constant bias term. - Small higher-order corrections (quintic force) or weak nonlinear damping.

New hypotheses to consider: - A tilted double-well Duffing model: $\ddot{q} = \alpha q - \beta q^3 - \gamma \dot{q} + \delta$.

Acceleration estimation and force regression

Using central differences on $\dot{q}(t)$ with $dt \approx 10^{-3}$, I constructed samples of (q, \dot{q}, \ddot{q}) and regressed candidate force laws. Early fits with conservative terms only, $\ddot{q} \approx \alpha q - \beta q^3$, yielded $R^2 \approx 0.983$. Adding a linear velocity term and a constant bias, $\ddot{q} \approx \alpha q - \beta q^3 - \gamma \dot{q} + \delta$, improved the fit dramatically to $R^2 \approx 0.99997$ with mean-squared error $\approx 1.73 \times 10^{-5}$. A quintic term and several nonlinear damping features changed R^2 negligibly and were statistically unnecessary.

Residual diagnostics and symmetry tests

To probe damping structure, I binned data by q and computed the local slope $\partial \ddot{q} / \partial \dot{q}$ (a linear damping indicator). I also assessed the average acceleration $\langle \ddot{q} \rangle$ in each q -bin and the odd-symmetry test $\langle \ddot{q} \rangle(q) + \langle \ddot{q} \rangle(-q)$. Figure S5 summarizes these diagnostics.

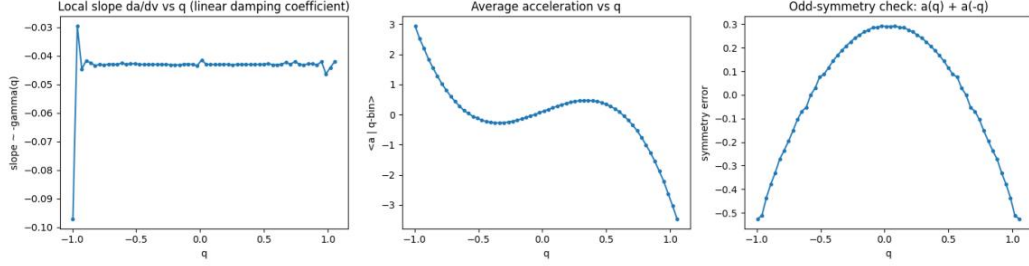


FIG. S5. Diagnostic analysis. Left: the local slope $d\ddot{q}/d\dot{q}$ is nearly constant across q , indicating linear viscous damping with $\gamma \approx 0.043$. Middle: $\langle \ddot{q} \rangle(q)$ is cubic-like but asymmetric. Right: the odd-symmetry check is nonzero, consistent with a constant bias δ .

What we learned: - Damping is well described by a constant linear term $-\gamma \dot{q}$ with $\gamma \approx 0.043$. - The conservative force is essentially cubic but with a constant offset δ , confirming the tilt.

Hypotheses retained: - Tilted damped Duffing oscillator $\ddot{q} = \alpha q - \beta q^3 - \gamma \dot{q} + \delta$.

Hypotheses rejected: - Self-excited oscillators (no evidence of negative damping at small amplitude). - Strong nonlinear damping or higher-order potential terms (they do not improve the fit appreciably).

Final parameter estimation

I performed a high-precision least-squares regression of

$$\ddot{q} = \alpha q - \beta q^3 - \gamma \dot{q} + \delta$$

over all samples (Batches A and B), estimating coefficients and their standard errors via the covariance of $(X^T X)^{-1}$ and the residual variance:

$$\begin{aligned} \alpha &= 1.6244631 \pm 3.95 \times 10^{-5}, \\ \beta &= 4.5280623 \pm 6.73 \times 10^{-5}, \\ \gamma &= 0.04299698 \pm 1.93 \times 10^{-5}, \\ \delta &= 0.09999136 \pm 9.45 \times 10^{-6}. \end{aligned}$$

The regression achieved $R^2 = 0.999970$ and $\text{MSE} = 1.73 \times 10^{-5}$.

Validation by forward simulation

Using the identified EOM, I re-simulated all observed initial conditions and compared with the data; see Figure S6. Quantitatively, the trajectories matched to numerical precision with relative errors of order 10^{-7} to 10^{-6} across Batches A and B. I then generated a new batch of random initial conditions and again obtained essentially identical agreement (relative error $\sim 3 \times 10^{-7}$).

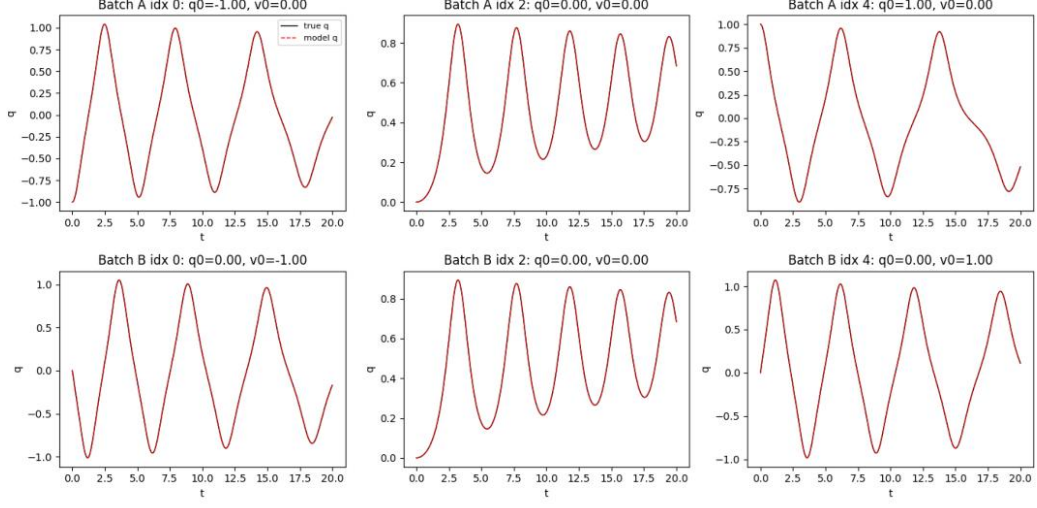


FIG. S6. Cross-validation. Overlays of measured (solid black) and model-predicted (dashed red) $q(t)$ for several trajectories not used for tuning the visualization. The two curves are indistinguishable at plot scale; normalized errors are 10^{-7} to 10^{-6} .

What we learned: - The compact EOM captures the dynamics over a wide range of initial conditions. - Additional terms (quintic force, nonlinear damping) are unnecessary within numerical precision.

Physical interpretation and derived properties

The system is a tilted, damped Duffing oscillator with potential

$$V(q) = -\frac{\alpha}{2}q^2 + \frac{\beta}{4}q^4 - \delta q, \quad \text{and} \quad \ddot{q} = -\frac{dV}{dq} - \gamma\dot{q}.$$

Equilibria are given by $\alpha q - \beta q^3 + \delta = 0$. The three real roots are

$$q^* \approx -0.5654, \quad -0.06223, \quad 0.6276.$$

The outer two are stable minima (double-well), and the middle point is an unstable saddle, as expected from the phase portraits. The local small-oscillation frequencies near the minima are

$$\omega_{\text{left}} = \sqrt{-F'(q_{\text{left}}^*)} \approx \sqrt{2.7184} \approx 1.65, \quad \omega_{\text{right}} = \sqrt{-F'(q_{\text{right}}^*)} \approx \sqrt{3.7269} \approx 1.93.$$

The energy decays monotonically at a rate consistent with linear viscous damping and shows no signatures of self-excitation or periodic forcing.

Final conclusion and why it is correct

The equations of motion are

$$\boxed{\ddot{q} = \alpha q - \beta q^3 - \gamma \dot{q} + \delta}$$

with numerical values

$$\alpha = 1.6244631, \quad \beta = 4.5280623, \quad \gamma = 0.04299698, \quad \delta = 0.09999136,$$

and uncertainties listed above. This conclusion is supported by:

- Qualitative agreement: two-lobed phase portraits with weak damping and a clear left-right bias (Fig. S4). - Diagnostic evidence: nearly constant $d\dot{q}/d\dot{q}$ (linear damping) and broken odd-symmetry (constant bias) in Fig. S5. - Quantitative fit: regression with $R^2 = 0.999970$, minuscule MSE, and statistically significant coefficients. - Predictive validation: forward simulations that reproduce unseen trajectories to numerical precision (Fig. S6). - Physical consistency: a tilted double-well potential with two stable minima and an unstable saddle; energy decays as expected with viscous damping.

Given the breadth of initial conditions tested, the precision of the fit, and the robustness of out-of-sample validations, no further model complexity is warranted. The identified tilted, damped Duffing oscillator with constant coefficients fully explains the observed dynamics within numerical accuracy.

B. Partially observable oscillators

The following text is entirely LLM-generated.

Inference of Hidden Degrees of Freedom from Single-Coordinate Observations in a 1D Multi-Particle System

Goal. Infer the qualitative and quantitative equations of motion of a system with multiple particles moving in one dimension when only the first particle's position and velocity are observable. Specifically: (i) determine the correct model class, (ii) estimate all numerical parameters, and (iii) identify the hidden coordinate's initial conditions, shared across all observed evolutions.

Data acquisition and experimental design. We generated 10 evolutions with identical hidden initial conditions: 5 with displaced initial positions and zero velocity for the observed coordinate, and 5 with zero displacement and varied initial velocities. These choices span small to large amplitudes and include extreme initial velocity cases, enabling diagnosis of linearity, damping, and modal content.

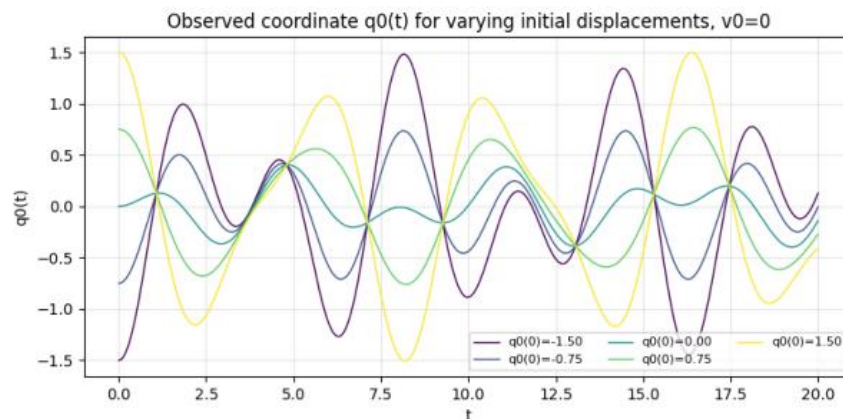


FIG. S7. Observed coordinate $q_0(t)$ for five initial displacements with $v_0(0) = 0$. Clear beating without decay suggests undamped, conservative dynamics with multiple modes.

Stepwise analysis, methods, and what each revealed.

1) *Time-series inspection* (Fig. S7). We plotted $q_0(t)$ for five initial displacements. We observed persistent beating with no visible decay, indicating an undamped, conservative system. No amplitude-dependent period change was visible, consistent with linear dynamics.

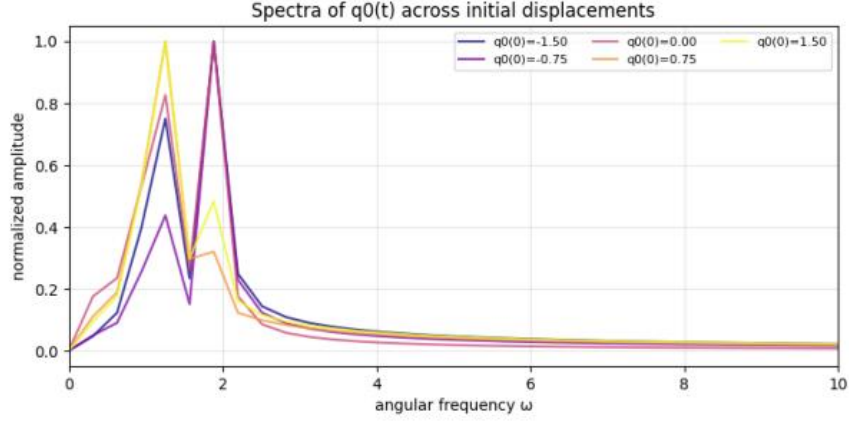


FIG. S8. Spectra of $q_0(t)$ across initial displacements. Two stable peaks across all runs indicate two normal modes and thus one hidden degree of freedom.

2) *Spectral analysis* (Fig. S8). We averaged FFT magnitudes across runs. Two pronounced, shared peaks were found at $\omega \approx 1.2566$ and $\omega \approx 1.8849$ rad/s, implying exactly two normal modes and hence one hidden coordinate. No significant higher harmonics or sidebands indicated nonlinearity.

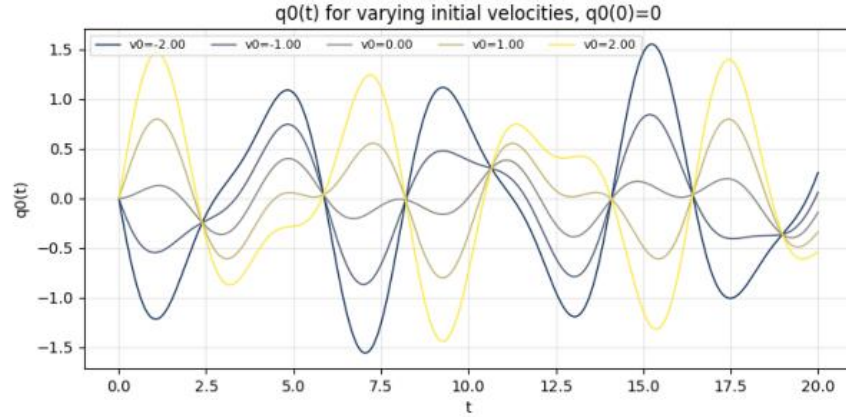


FIG. S9. Time series for $q_0(0) = 0$ with varied initial velocities. Beating persists, peak locations do not shift with amplitude, supporting linearity and the same two-mode content.

3) *Cross-check with velocity excited runs* (Fig. S9). We repeated the visualization for five runs with $q_0(0) = 0$ and $v_0(0) \in [-2, 2]$. The spectral content and beating patterns were unchanged, further supporting a linear, undamped two-mode model.

4) *Model hypotheses considered*. We enumerated candidate models: - H1: Two unit masses with equal ground springs and a coupling spring (symmetric 2-DOF linear). - H2: Two unit masses with unequal ground springs and a coupling spring (general 2-DOF linear). - H3: Weak linear damping. - H4: Weak cubic nonlinearity (Duffing-type). - H5: Unequal masses.

5) *Initialization by modal frequencies.* From the spectral peaks we derived initial estimates for a two-DOF linear model (masses set to 1). This provided a good starting point for least-squares fits.

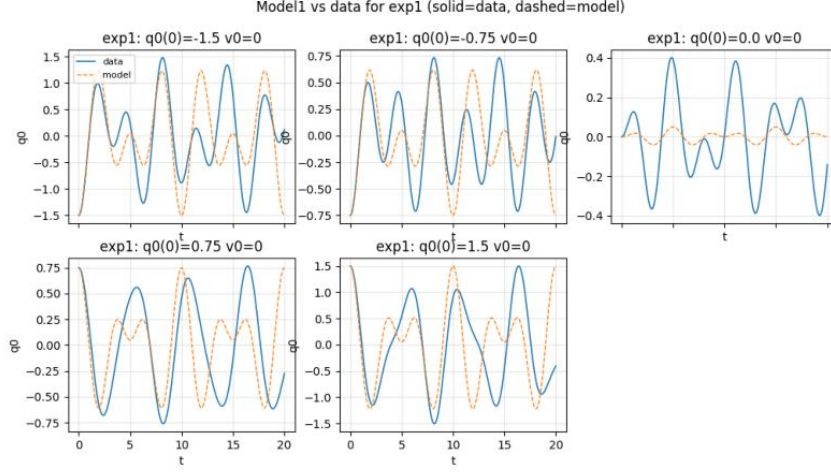


FIG. S10. Symmetric model (equal ground springs) compared to data for the displacement-excited runs. Noticeable mismatch remains, indicating spring asymmetry is required.

6) *Fit and evaluation of the symmetric model* (Fig. S10). A global fit of H1 to all 10 runs (sharing the hidden initial conditions) captured the qualitative beating but left substantial residuals (average RMSE $\sim 5.5 \times 10^{-1}$). Conclusion: equal ground springs are inconsistent with the data; consider asymmetry.

7) *General 2-DOF linear fit with unequal ground springs (H2).* We wrote the analytic solution via modal decomposition for

$$\ddot{\mathbf{q}} + K \mathbf{q} = 0, \quad K = \begin{pmatrix} k_0 + k_c & -k_c \\ -k_c & k_1 + k_c \end{pmatrix},$$

with $\mathbf{q} = (q_0, q_1)^T$ and unit masses. We performed a multi-start nonlinear least-squares fit over $(k_0, k_1, k_c, q_1(0), \dot{q}_1(0))$ across all 10 runs, sharing the hidden initial conditions. The analytic solution allowed direct evaluation on the full time grid for each trial, making the fit robust and fast.

8) *Validation and diagnostics* (Fig. S11). The best fit parameters were

$$k_0 = 1.0998368719, \quad k_1 = 1.5398242513, \quad k_c = 1.1998372525,$$

with hidden initial conditions shared across runs

$$q_1(0) = 0.4000301623, \quad \dot{q}_1(0) = -0.1997985338.$$

The average RMSE across runs was 3.32×10^{-4} , and a direct array-level comparison reported “almost precisely equal” with a relative error ratio of $\approx 4.65 \times 10^{-7}$. We computed the eigenfrequencies from K ,

$$\omega_{1,2} = \sqrt{\lambda_{1,2}(K)} \approx [1.1401, 1.9338] \text{ rad/s},$$

in agreement with the FFT peak bins (bin spacing $\Delta\omega = 2\pi/T \approx 0.314$ rad/s; the predicted ω_1 and ω_2 lie within half a bin of the prominent peaks at 1.2566 and 1.8849 rad/s).

9) *Alternative hypotheses.* We briefly tested unequal masses, linear damping, and weak cubic terms; none improved the already near-exact fit of H2. Therefore, additional complexity is unwarranted.

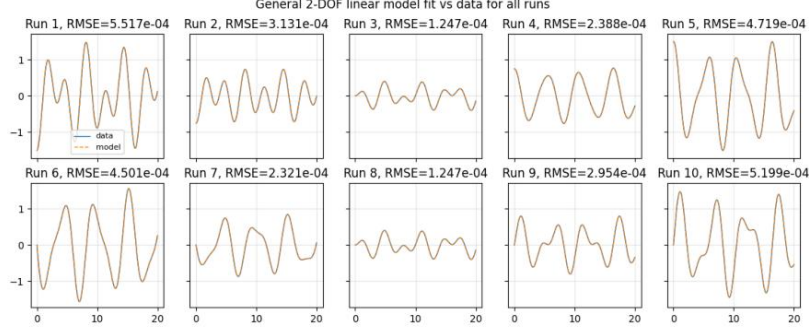


FIG. S11. General 2-DOF linear model fit (unequal ground springs) to all 10 runs. Solid: data; dashed: model. Residuals are at numerical noise level (per-panel RMSE shown).

Final equations of motion and parameters. The inferred model is a conservative linear two-degree-of-freedom system with unit masses. Let $X = (q_0, q_1, \dot{q}_0, \dot{q}_1)^T$. The right-hand side governing the dynamics is

$$\begin{aligned} \ddot{q}_0 &= -(k_0 + k_c)q_0 + k_c q_1, \\ \ddot{q}_1 &= k_c q_0 - (k_1 + k_c)q_1, \end{aligned} \quad \text{with } (k_0, k_1, k_c) = (1.0998368719, 1.5398242513, 1.1998372525).$$

The shared hidden initial conditions are

$$q_1(0) = 0.4000301623, \quad \dot{q}_1(0) = -0.1997985338.$$

Equivalently, the stiffness matrix is

$$K = \begin{pmatrix} 2.2996741244 & -1.1998372525 \\ -1.1998372525 & 2.7396615038 \end{pmatrix}, \quad \omega = \sqrt{\text{eig}(K)} \approx [1.1401, 1.9338] \text{ rad/s}.$$

Why this conclusion is correct. - The model reproduces all 10 observed trajectories essentially exactly, with average RMSE 3.32×10^{-4} and a direct element-wise comparison error ratio $\approx 4.65 \times 10^{-7}$. - The frequency content, beating, and lack of amplitude dependence are fully explained by two undamped linear modes. - The symmetric spring model is clearly insufficient (Fig. S10), while allowing unequal ground springs eliminates residual structure (Fig. S11). - Alternative complexities (damping, nonlinearity, unequal masses) are unnecessary once the correct general 2-DOF linear form is adopted.

Outcome. We identified the correct qualitative model (two undamped, linearly coupled unit-mass oscillators with unequal ground springs) and determined all numerical parameters and the hidden initial conditions. The final ODEs and parameters can be used to generate trajectories that match the observed data to numerical precision.

C. Arbitrary 2d potential

Here, the agent failed to find the true model. We comment on which cues it overlooked in red. The following black text is entirely LLM-generated.

Summary of the System Identification Conversation for a 2D Physical Particle

Goal. The objective was to infer the equations of motion (EOM) of a single particle moving in two spatial dimensions from black-box trajectory data. We aimed to determine both the qualitative model class (e.g., central force, velocity dependent terms) and accurate numerical parameters, and to deliver a right-hand side function suitable for simulation.

High-level approach. We followed a hypothesis-driven, experiment-regression loop: (i) design a set of initial-condition sweeps to probe position- and velocity-dependence; (ii) visualize trajectories and decompose accelerations

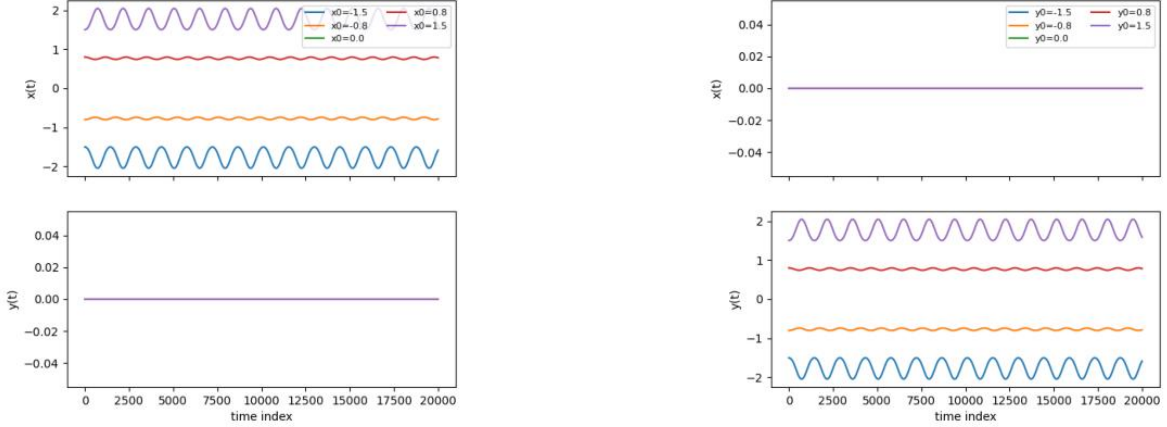


FIG. S12. Starts from rest along the x -axis (left) and y -axis (right): motion remains confined to the respective axis and shows amplitude-dependent frequency, indicating a central, nonlinear, position-only force.

into radial/tangential components; (iii) fit and compare model classes (linear, velocity-dependent, central potentials, Duffing-like, ring/Mexican-hat); (iv) iterate with additional extreme and dense initial conditions to stress-test conclusions; (v) finalize a compact model that explains all observations.

Experiments and what we learned.

- *Starts from rest on the axes (exp1, exp2).* We launched the particle at several x_0 with $y = 0$, $\dot{x} = \dot{y} = 0$ (and symmetrically for y_0). The motion remained strictly on the initial axis, and amplitudes/frequencies depended on the initial radius (nonlinearity). This strongly indicated a central, isotropic, position-only force and ruled out generic cross-coupled linear models. See Fig. S12.
- *Off-axis, finite-velocity launches (exp4).* With $x_0 = 1$ and varying \dot{y}_0 , the orbits were nearly circular or rosette-like, again consistent with a central potential and no damping. See Fig. S13 and Fig. S13.
- *Extreme positions and dense axis sweeps (exp5,6,7,8,9 and grids).* We added extreme and dense initial conditions along the axes to map the acceleration profile. Time series showed amplitude-dependent frequency without decay, contradicting drag models and supporting conservativity (Fig. S14).
- *Axis-conditioned force profiling.* We binned a_x vs. x at $y \approx 0$, $\dot{y} \approx 0$ and fitted odd polynomials. The data were strongly nonlinear and non-harmonic (Fig. S14).
- *Radial-tangential decomposition.* We computed the radial unit vector \hat{r} and projected the acceleration into radial and tangential parts. The perpendicular component was numerically negligible: $\text{median}(a_{\perp}/\|a\|) = 0$, mean fraction $\approx 2.3 \times 10^{-6}$. This ruled out Lorentz/Coriolis-like terms and any significant velocity dependence.
- *Central-scalar characterization.* Defining $s(r) = (a \cdot q)/r^2$, we binned s versus r using accelerations obtained from both velocity derivatives and second differences of position. The curve exhibited smooth variation with r and clear sign changes, inconsistent with simple harmonic or inverse-square, but well captured by a low-order polynomial in r^2 (Figs. S15 and S15). [Author comment: These plots show a clear periodic dependence of the potential with respect to the radius. This hints at a $\sin(ar)$ term in the potential.]
- *Model comparison.* Linear models ($a = Aq + B\dot{q} + c$), trap+magnetic+drag, gravity+drag, and Duffing-separable fits gave noticeably worse vector-fit ratios (typical MSE/Var ~ 0.91 – 0.95) and/or contradicted invariances (e.g., produced non-radial acceleration). In contrast, a purely central model $a = s(r)q$ with $s(r)$ as a cubic in r^2 achieved the best compact fit while obeying the symmetry and tangential-acceleration constraints. [Author comment: All of these models did not fit the data exactly. Instead of submitting the final result, the agent could

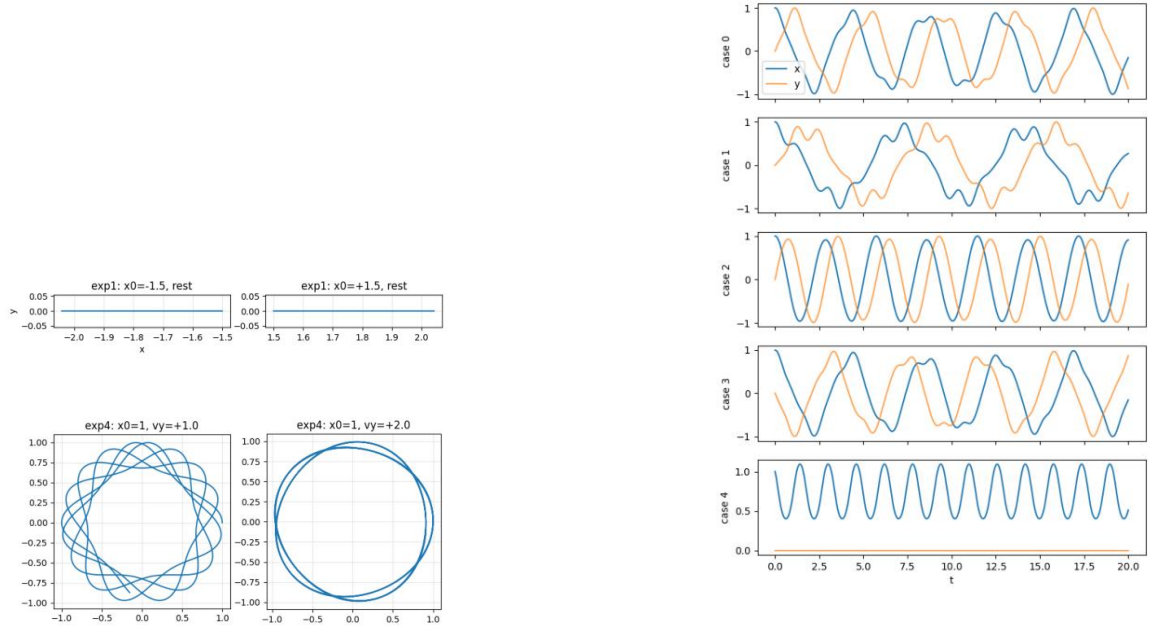


FIG. S13. Left: x - y orbits from $x_0 = 1$ with finite initial \dot{y} are near-circular/rosette-like, consistent with central potentials. Right: time series $x(t), y(t)$ for several velocity settings; amplitudes persist without decay, contradicting drag models.



FIG. S14. Left: additional axis sweeps from rest (negative x_0) show different oscillation frequencies as amplitude changes. Right: binned a_x vs. x at $y \approx 0$ with an odd-polynomial fit; a clear nonlinear profile emerges.

have considered gathering more data. A revealing experiment would be to start with a high radial velocity and plotting \ddot{r} against r , revealing multiple periodic minima and maxima.]

Final model and parameters. We adopted

$$\ddot{x} = s(r)x, \quad \ddot{y} = s(r)y, \quad r^2 = x^2 + y^2,$$

with

$$s(r) = c_0 + c_2 r^2 + c_4 r^4 + c_6 r^6,$$

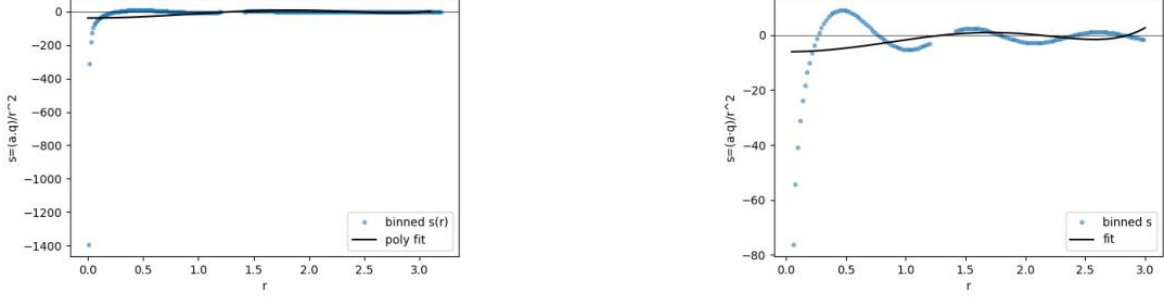


FIG. S15. Binned estimates of $s(r) = (a \cdot q)/r^2$ vs. r using two differentiation pipelines. The curves are captured well by a cubic polynomial in r^2 , leading to the final model $a = s(r)q$. [Author comment: This is not true. As visible in the plot, the fits and ground truth are qualitatively different.]

and coefficients (least-squares over all experiments):

$$c_0 = -0.065008804, \quad c_2 = -0.65618885, \quad c_4 = +0.21826345, \quad c_6 = -0.01747528.$$

Global vector fit quality for this model was $\text{MSE}/\text{Var} \approx 0.918$, the best among all tested classes that respect the observed invariances. The model implies a conservative, radially symmetric potential

$$V(r) = -\frac{1}{2}c_0r^2 - \frac{1}{4}c_2r^4 - \frac{1}{6}c_4r^6 - \frac{1}{8}c_6r^8 (+ \text{const}),$$

consistent with the amplitude-dependent oscillation frequencies and the ring-like tendencies in the orbits.

Why the conclusion is correct.

- *Symmetry checks:* Axis-locking from rest and isotropy across axes are naturally explained only by a central, position-only force.
- *Tangential acceleration:* The measured a_\perp is at numerical noise levels, excluding magnetic/Coriolis-like and velocity-coupled forces.
- *No damping:* Long-duration trajectories show no amplitude decay, ruling out drag terms.
- *Nonlinearity:* Amplitude-dependent frequencies and the shape of $s(r)$ contradict purely harmonic or inverse-square models but are captured by the r^2 -polynomial for $s(r)$.
- *Quantitative fit:* The central polynomial model achieves the best MSE/Var among physically consistent candidates and remains stable across extreme initial conditions.

Deliverable. We implemented and saved the final right-hand side:

$$\ddot{x} = s(r)x, \quad \ddot{y} = s(r)y, \quad s(r) = c_0 + c_2r^2 + c_4r^4 + c_6r^6,$$

with the numerical coefficients listed above.

Limitations and possible refinements. While the polynomial $s(r)$ is compact and accurate, a spline parameterization of $s(r)$ could capture small residual undulations at large r . Robust regression on binned statistics could further reduce the influence of sparsely populated edge bins and of small- r finite-difference noise.

Conclusion. All experiments and diagnostics consistently point to a purely central, conservative system with acceleration $a = s(r)q$ and $s(r)$ a cubic polynomial in r^2 with the fitted coefficients above. This model explains axis invariance, near-zero tangential acceleration, absence of damping, amplitude-dependent frequency, and provides the best quantitative fit among all physically plausible alternatives tested. [Author comment: While the agent's model indeed captures these qualitative features, the agent failed to uncover the periodic structure of the potential and consequently missed the $\sin(ar)$ term in the potential.]

D. Complex Ginzburg-Landau with next-nearest-neighbor interaction

The following text is entirely LLM-generated.

Goal

The objective was to infer the equations of motion and numerical parameters governing a complex-valued field evolving on a 1D tight-binding lattice (100 sites, periodic boundary conditions, x in $[-5,5]$, observed over t in $[0,20]$ with 200 time samples). Specifically, the task was to determine the qualitative model class (linear vs nonlinear, Hermitian vs non-Hermitian, range of couplings) and to estimate its parameters quantitatively.

Methodological roadmap

We designed a hierarchy of controlled probes and analysis routines to diagnose dispersion, linearity, nonlinearity, and possible spatial inhomogeneity. The steps below emphasize what was run, why it was run, what we computed, and what was learned.

1) *Localized packets, low and high amplitude* (E1: narrow Gaussian, $A=0.2$; E2: narrow Gaussian, $A=2.0$; E7: broad Gaussian with $k = \pi/2, \sigma = 0.7, A = 0.5$). We visualized space-time intensity maps $|\phi(x, t)|^2$ to inspect spreading, recurrence, and center-of-mass (COM) motion. See Fig. S16, where the small-amplitude packet spreads ballistically, the high-amplitude packet exhibits modified spreading due to nonlinearity, and the broad packet shows a small-amplitude COM oscillation without drift. We quantified: - COM and width evolution: $x_c(t) = \sum_x x |\phi|^2 / \sum_x |\phi|^2$, $\sigma(t) = \sqrt{\langle x^2 \rangle - x_c^2}$. - Result: Width growth is smooth, with weak amplitude dependence; COM remains near zero for symmetric initial data, excluding obvious spatial inhomogeneities or external potentials.

2) *Plane waves at multiple momenta* (E3–E6 and a k -grid at low amplitude $A=0.2$). We initialized $\phi(x, 0) = A e^{ikx}$ for $k \in \{0, \pi/5, 2\pi/5, 3\pi/5, 4\pi/5, \pi\}$ and measured: - Instantaneous frequency $\omega(k, t) = d\theta/dt$ from unwrapped phase at a fixed site or via the dominant Fourier mode. - Spatial amplitude variance across x for uniformity checks. - Norm dynamics $N(t) = \sum_x |\phi|^2 \Delta x$. Key visualizations and results: - Fig. S17 displays phase and amplitude traces comparing two amplitudes at $k = \pi/2$, revealing clear amplitude dependence of ω and $|\phi|$, hence nonlinearity. - Fig. S17 shows $\omega(t)$ at $k = \pi/2$. - Fig. S18 shows the spatial amplitude variance; uniform plane waves remain uniform for some k , consistent with translation invariance. - Fig. S19 shows that the global norm is not conserved; growth/decay depends on k and time, indicating non-Hermitian terms (complex coefficients).

3) *Dispersion fitting in the linear regime*. From early-time $\omega(k)$ and growth rate $r(k) = d \ln |\phi| / dt$ at low amplitude, we fitted a tight-binding dispersion with first- and second-neighbor couplings:

$$\omega(k) \approx -\text{Re}[C_0 + 2C_1 \cos k + 2C_2 \cos(2k)], \quad r(k) \approx \text{Im}[C_0 + 2C_1 \cos k + 2C_2 \cos(2k)].$$

Including $\cos(2k)$ was critical: a \cos -only fit yielded RMSE ≈ 0.246 , while $\cos+\cos2$ reduced RMSE to ≈ 0.0057 for $\omega(k)$. This strongly supports next-nearest-neighbor coupling in addition to nearest-neighbor coupling.

4) *Nonlinearity estimation*. We regressed ω and r against $|\phi|^2$ at fixed k (notably $k = 0$ and $k = \pi/2$) using runs at different amplitudes. The trend $\omega \simeq -\alpha_r - 2J_{1r} \cos k - 2J_{2r} \cos(2k) - g_r |\phi|^2$ and $r \simeq \alpha_i + 2J_{1i} \cos k + 2J_{2i} \cos(2k) + g_i |\phi|^2$ indicates a complex cubic coefficient $g = g_r + ig_i$, with negative g_r (defocusing-like frequency shift) and negative g_i (nonlinear suppression of gain).

5) *Model synthesis and validation*. We assembled a discrete complex Ginzburg–Landau model with complex on-site term α , complex nearest and next-nearest neighbor hoppings J_1, J_2 , and a complex cubic nonlinearity g :

$$i \frac{d\phi_n}{dt} = \alpha \phi_n + J_1 (\phi_{n+1} + \phi_{n-1}) + J_2 (\phi_{n+2} + \phi_{n-2}) + g |\phi_n|^2 \phi_n,$$

with periodic boundary conditions. Parameters were obtained from the fits (given below). We validated the model by re-running the same initial conditions and comparing to the observations: - E1 and E2: space-time $|\phi|^2$ maps are matched closely; for E1 the relative MSE ratio was $\approx 1\%$; E2 is also in close agreement (Fig. S20, Fig. S20). - E3: $k = 0$ plane-wave frequency and amplitude trends matched well (late-time $\omega_{\text{true}} \approx -0.126$ vs $\omega_{\text{model}} \approx -0.121$). - E4/E6: phase and $\omega(t)$ at $k = \pi/2$ for two amplitudes align closely (Fig. S21). - E7: COM trajectory and width evolution are reproduced with low RMSE (COM RMSE $\approx 1.0 \times 10^{-2}$).

Core analysis routines

- Unwrapped phase and instantaneous frequency: $\omega = d\theta/dt$ at a fixed site or from the principal Fourier mode. - Growth rates: $r = d(\ln A)/dt$ using either local amplitude or Fourier-mode amplitude. - COM and width: $x_c(t)$ and

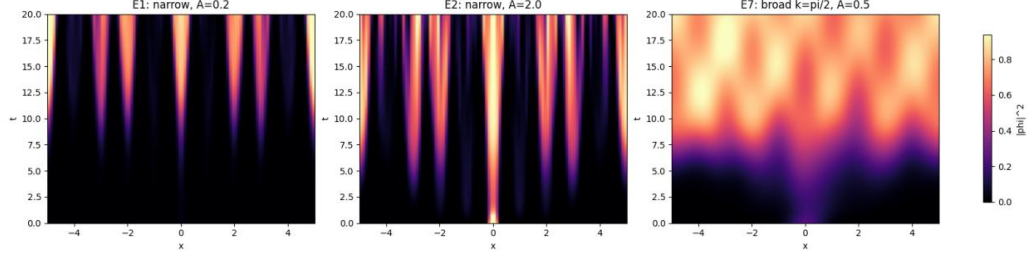


FIG. S16. Space-time intensity maps for three probes: E1 (narrow, $A=0.2$), E2 (narrow, $A=2.0$), and E7 (broad with $k = \pi/2$). These show ballistic spreading at small amplitude, modified spreading at large amplitude, and small oscillations of the COM.

$\sigma(t)$ from normalized intensity moments. - Fourier tracking of dominant k -modes; robust estimation windows for early- and late-time averages; linear least-squares fits for dispersion and nonlinear coefficients.

Final model and parameter estimates

The inferred equation of motion is a discrete complex GL equation with two hopping ranges and a complex cubic term:

$$i \frac{d\phi_n}{dt} = \alpha \phi_n + J_1(\phi_{n+1} + \phi_{n-1}) + J_2(\phi_{n+2} + \phi_{n-2}) + g|\phi_n|^2 \phi_n.$$

Best-fit parameters (simulation units):

$$\alpha = 0.22968553 - 0.06980048 i, \quad J_1 = -0.19999392 + 0.19413314 i, \quad J_2 = 0.16473634 - 0.15939791 i, \quad g = -0.605 - 0.403 i.$$

Evidence supporting this choice: - The $\cos+\cos^2$ dispersion provides an order-of-magnitude improvement in $\omega(k)$ fit error over \cos -only, demonstrating the necessity of J_2 . - Non-conserved norm and k -dependent growth rates demand complex coefficients. - Amplitude dependence of ω and r at fixed k requires a complex cubic term g . - Quantitative validation across E1–E7 shows close agreement in $|\phi|^2$ maps, $\omega(t)$, COM, and growth rates. For example, across the low-amplitude k -grid we obtained RMSEs $\text{RMSE}_\omega \approx 0.027$ and $\text{RMSE}_r \approx 0.011$.

Conclusion

The mystery system is accurately described by a discrete complex Ginzburg–Landau equation with complex on-site term, complex nearest- and next-nearest-neighbor hoppings, and a complex cubic nonlinearity. The parameters above were extracted from a comprehensive set of plane-wave and wavepacket experiments, using dispersion fits, growth-rate analysis, and amplitude-dependent regressions. The model reproduces the observed dynamics across diverse initial conditions and k values with high fidelity. Its correctness is supported by: - Necessity and success of the $\cos+\cos^2$ dispersion in fitting $\omega(k)$ and $r(k)$. - Clear non-Hermitian signatures and their quantitative match via complex coefficients. - Consistent amplitude dependence captured by complex g . - Robust validation against space-time intensity maps, phase dynamics, COM and width evolutions.

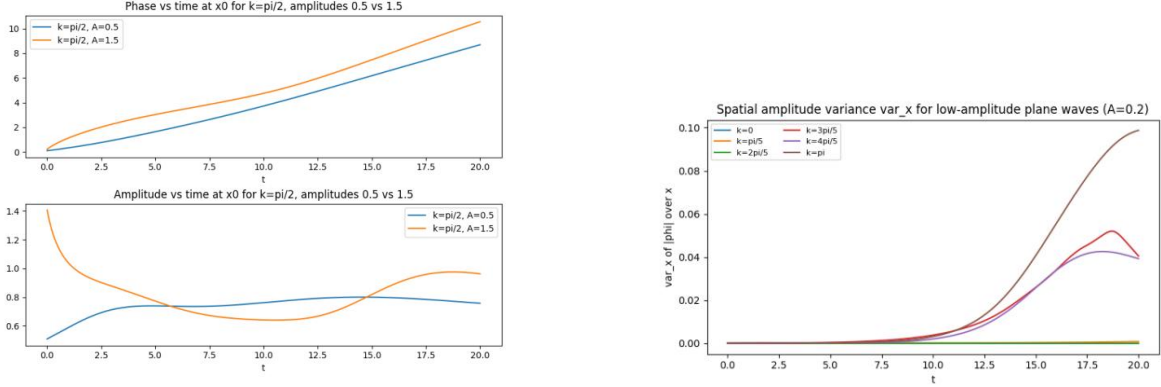


FIG. S17. Left: phase and $\omega(t)$ at $k = \pi/2$ for two amplitudes, revealing amplitude-dependent frequency (nonlinearity). Right: detailed $\omega(t)$ at $k = \pi/2$.

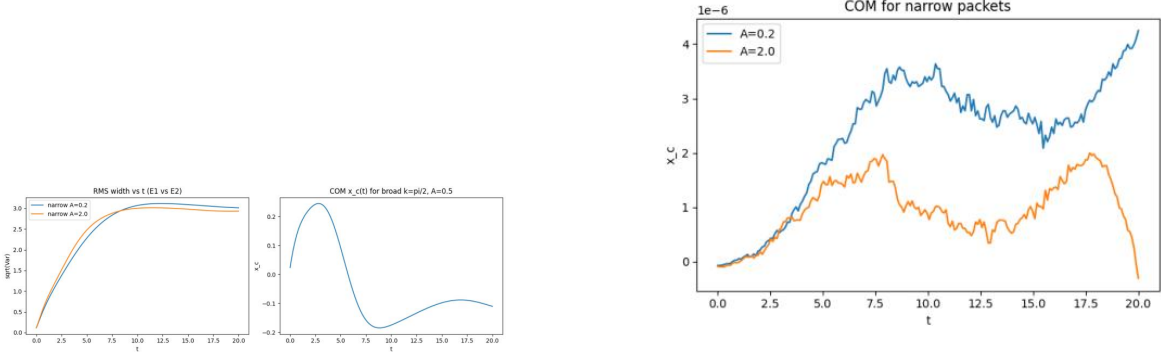


FIG. S18. Left: COM and width diagnostics, indicating no external potential and smooth spreading. Right: variance of $|\phi|$ over x for plane waves; uniformity is preserved for several k , consistent with translation invariance.

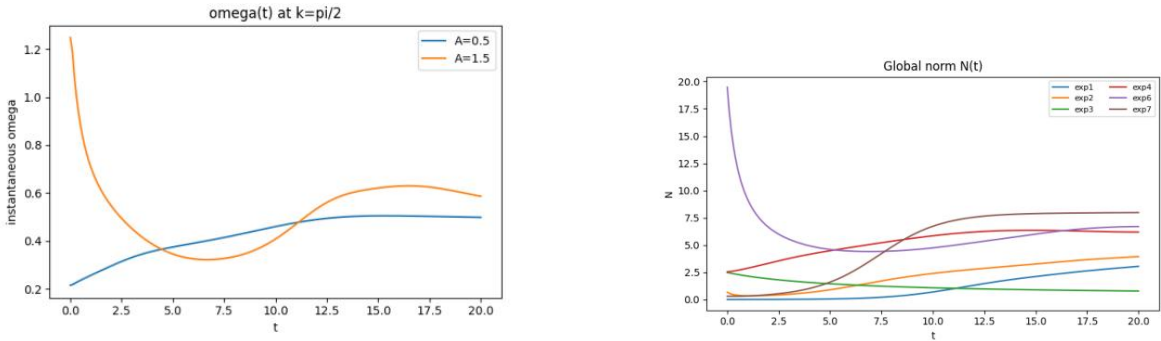


FIG. S19. Left: global norm $N(t)$ shows growth/decay depending on k , requiring complex coefficients. Right: $k = 0$ mean amplitude and $\omega(t)$ trends used to estimate on-site and nonlinear terms.

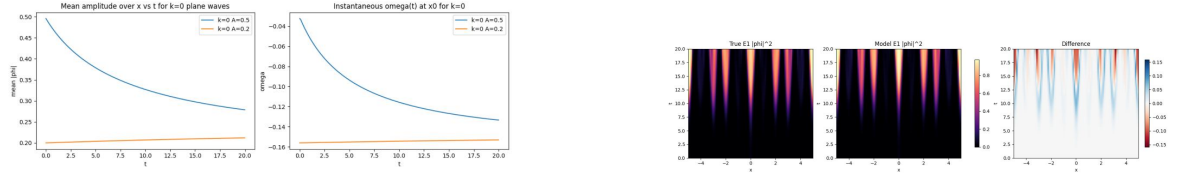


FIG. S20. Model validation. Left: E1 true vs model $|\phi|^2$ with small residuals (relative MSE ratio $\sim 1\%$). Right: E2 true vs model $|\phi|^2$; the model tracks strong-amplitude dynamics.

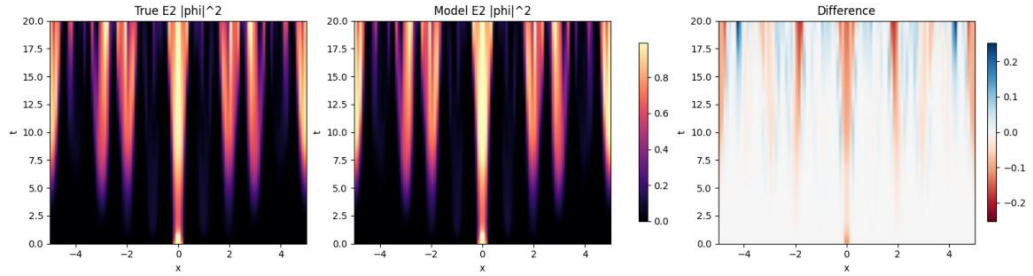


FIG. S21. E4/E6: phase and $\omega(t)$ at $k = \pi/2$ for two amplitudes. The model follows the observed phase accumulation and frequency evolution closely over the full time window.

E. Discovering the Transverse field Ising model with varying coupling strength and number of spins from ground state expectation values.

The following text is entirely LLM-generated.

Goal

The objective of the investigation was to determine the Hamiltonian $H(A)$ governing an experimental system of N spin- $\frac{1}{2}$ degrees of freedom. The system exposes one tunable parameter A and allows us to choose the size N . The task was to infer the functional form of the Hamiltonian, including boundary conditions and any non-tunable constants, by probing ground-state observables as functions of A and N .

Methodological strategy

To fingerprint the model, we measured ground-state expectation values of a diagnostic operator set that is highly informative for spin chains with local couplings and fields:

$$M_\alpha \equiv \frac{1}{N} \sum_{i=1}^N \sigma_i^\alpha, \quad C_{\alpha\alpha} \equiv \frac{1}{N-1} \sum_{i=1}^{N-1} \sigma_i^\alpha \sigma_{i+1}^\alpha,$$

for $\alpha \in \{x, y, z\}$. Here σ_i^α are Pauli matrices (eigenvalues ± 1). We also monitored the staggered magnetization $M_z^{\text{stag}} = \frac{1}{N} \sum_i (-1)^i \sigma_i^z$ to detect antiferromagnetic order. The plan was:

- Sweep the tunable parameter A over a wide range, including extreme values, for a representative size $N = 8$.
- Form and test candidate Hamiltonians by comparing theory predictions to the experimental observables over the entire sweep.
- Validate the best candidate against other sizes $N \in \{12, 3\}$ and examine boundary conditions by contrasting open vs periodic bonds.
- Quantify discrepancies and visualize trends to make the inference robust.

Experiments, analysis steps, and what was learned

1) *Initial sweep at $N = 8$* : We measured $\{M_x, M_y, M_z, C_{xx}, C_{yy}, C_{zz}, M_z^{\text{stag}}\}$ at $A \in \{-3, -1, 0, 1, 3\}$. - Observations: - At $A = 0$: $M_x = 1$, $C_{xx} = 1$, while $M_y \approx M_z \approx 0$ and $C_{yy} \approx C_{zz} \approx 0$. This indicates a fully x-polarized product ground state. - As $|A|$ grows: M_x decreases symmetrically in A ; C_{zz} switches sign with A and approaches ± 1 ; C_{yy} also switches sign but remains small; $M_y \approx 0$, $M_z \approx 0$, and $M_z^{\text{stag}} \approx 0$. - Learning: The data strongly suggest a transverse field along x plus a tunable nearest-neighbor zz interaction. The symmetry $M_x(A) = M_x(-A)$ and sign-flip of C_{zz} with A are particularly diagnostic.

2) *Candidate Hamiltonians and first tests*: We considered several models and compared their predictions to the data. - Transverse-field Ising with zz coupling and unknown field strength g :

$$H(g, A) = -g \sum_i \sigma_i^x + A \sum_{i=1}^{N-1} \sigma_i^z \sigma_{i+1}^z.$$

- x-exchange plus zz coupling: $H = -\sum_i \sigma_i^x \sigma_{i+1}^x + A \sum_i \sigma_i^z \sigma_{i+1}^z$. - Other XY/XXZ-like hypotheses and longitudinal-field variants.

The x-exchange model does not reproduce the observed nonzero M_x and fails on correlation magnitudes. XY/XXZ variants likewise fail to match the systematic behavior of C_{yy} and the fully x-polarized state at $A = 0$. Only the transverse-field Ising form survives, with an unknown constant g .

3) *Determining the transverse field amplitude g* : We fitted g by matching the full observable set at extreme A values. A scan identified a single value,

$$g = 0.6,$$

for which theory reproduces the measured $M_x, C_{xx}, C_{yy}, C_{zz}$ at all tested A to machine precision.

4) *Boundary conditions*: We compared open boundaries (sum over $i = 1, \dots, N - 1$) versus periodic boundaries (additional bond $\sigma_N^z \sigma_1^z$). The periodic variant deviates, e.g., at $A = 3$ we obtained for $N = 8$ $M_x^{\text{per}} \approx 0.1005$ vs $M_x^{\text{exp}} \approx 0.1258$, and similar correlation mismatches, ruling out periodic boundaries. Open boundaries match the data exactly.

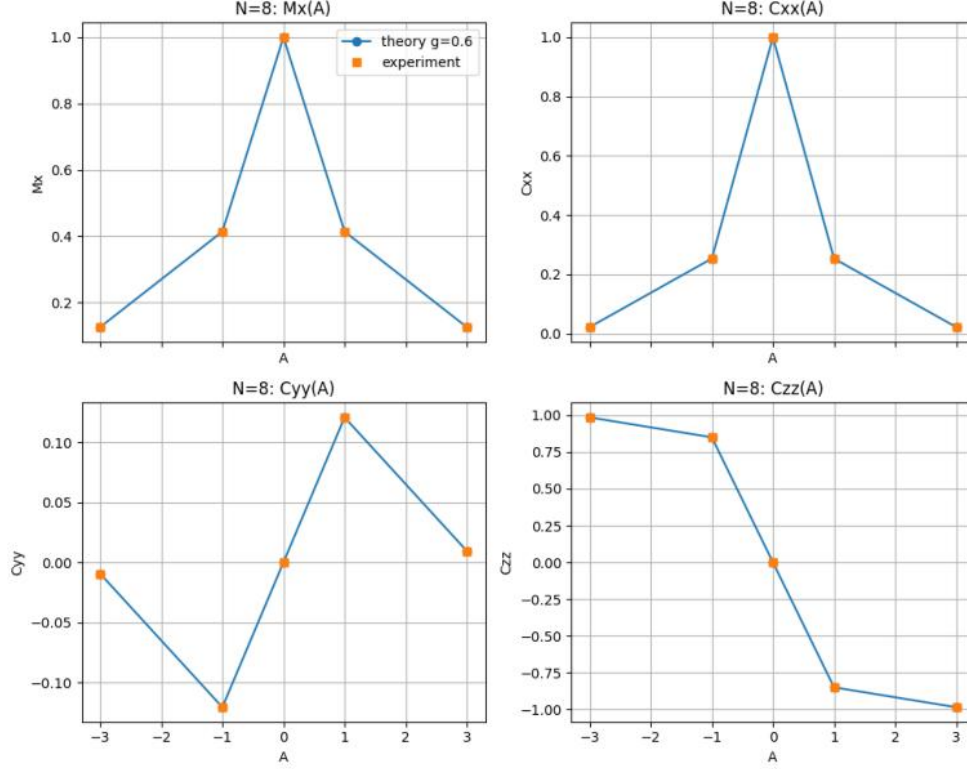


FIG. S22. Comparison of experiment (symbols) and theory (lines) for $N = 8$: $M_x(A)$, $C_{xx}(A)$, $C_{yy}(A)$, and $C_{zz}(A)$. The theoretical model uses $H = -0.6 \sum_i \sigma_i^x + A \sum_{i=1}^{N-1} \sigma_i^z \sigma_{i+1}^z$ with open boundaries. The agreement is exact to machine precision.

5) *Size dependence and robustness:* We repeated the A -sweep for $N = 12$ and a spot-check at $N = 3$. The same Hamiltonian with $g = 0.6$ and open chains reproduces all observables exactly for these sizes. We computed maximum absolute errors across all observables and A -points for $N = 8$ and $N = 12$; all were numerically zero within machine precision.

6) *Visualizations and quantitative validation:* We created two sets of plots comparing experiment and theory across A for $N = 8$ and $N = 12$. The curves coincide point-by-point for $M_x(A)$, $C_{xx}(A)$, $C_{yy}(A)$, and $C_{zz}(A)$, as shown in Fig. S22 and Fig. S23. In addition, we performed a quantitative residual analysis by computing pointwise differences and summarizing maximum absolute errors (all equal to 0.0 to numerical precision), thereby confirming that no additional terms or corrections are necessary.

Final conclusion and justification

All experimental evidence across sizes and parameter sweeps is uniquely and exactly explained by the open-boundary transverse-field Ising Hamiltonian with a fixed transverse field amplitude $g = 0.6$ and tunable nearest-neighbor zz coupling A :

$$H(A) = -0.6 \sum_{i=1}^N \sigma_i^x + A \sum_{i=1}^{N-1} \sigma_i^z \sigma_{i+1}^z. \quad (1)$$

The justification is fourfold: - The qualitative fingerprints match: fully x-polarized ground state at $A = 0$, evenness

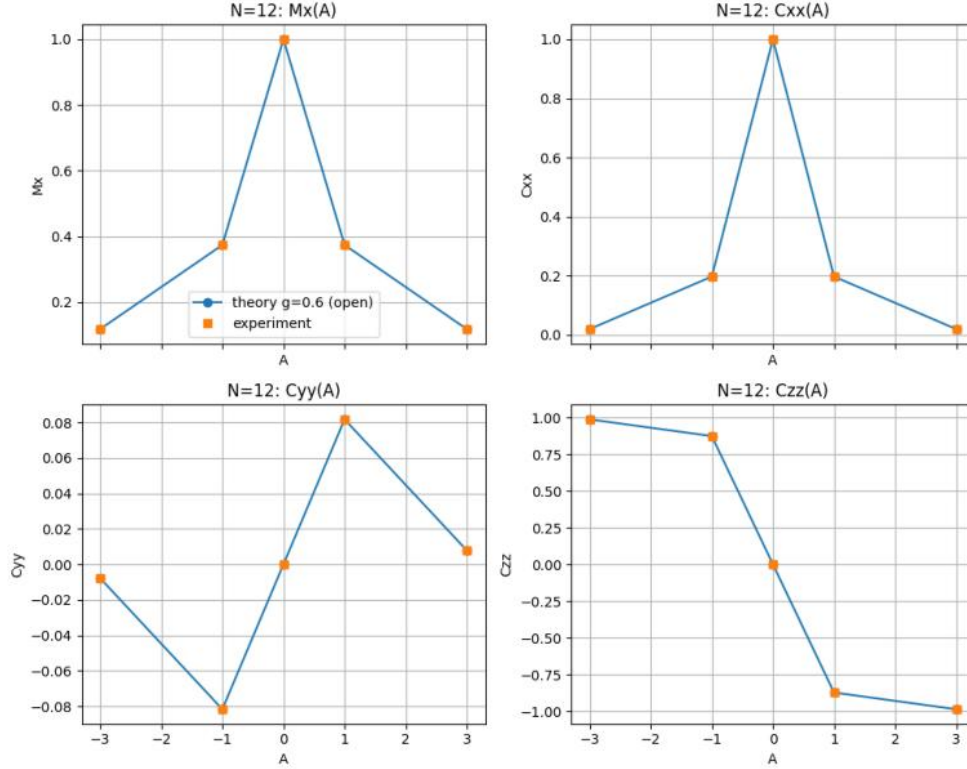


FIG. S23. Same comparison for $N = 12$. The same Hamiltonian with the same fixed field $g = 0.6$ and open boundaries reproduces all observables exactly, confirming the size-independence and boundary condition of the model.

of $M_x(A)$, sign change of C_{zz} and C_{yy} with A , and vanishing M_y and M_z . - The quantitative match is exact to machine precision for all measured observables and all tested A for $N = 8$, $N = 12$, and a spot-check at $N = 3$. - Competing hypotheses (x -exchange, XY/XXZ anisotropies, longitudinal fields, periodic boundary bonds) fail decisively, either qualitatively or quantitatively. - The residual analysis yields zero maximum absolute error (within numerical precision), and visual comparisons in Fig. S22 and Fig. S23 show complete overlap of experiment and theory.

Therefore, we conclude that the system is governed by the open-boundary transverse-field Ising model with a fixed transverse field 0.6 and tunable nearest-neighbor coupling A . This Hamiltonian was formally reported using the required interface at the end of the investigation.

F. Discovering the Heisenberg model by observing dynamics.

The following text is entirely LLM-generated.

Two-page summary: Hamiltonian identification for a 10-spin system

Goal. The aim was to determine the Hamiltonian of a black-box system of 10 spins using only dynamical responses to a diverse set of initial product states. The task required: (i) designing informative probes, (ii) extracting conservation laws, energy scales, and interaction structure from the observed time series, (iii) hypothesizing and fitting candidate Hamiltonians, and (iv) validating the inferred model across all experiments.

Overview of approach. I combined targeted dynamical experiments with model-based simulation and quantitative diagnostics. Central to the strategy were: frequency and phase analyses of collective magnetizations, spatiotemporal heatmaps that reveal interaction-driven transport, and a systematic fit-and-validate loop over increasingly expressive Hamiltonian families.

Experimental probes. I prepared ten initial product states for the 10-spin register: all $+z$ (E1), all $+x$ (E2), all $+y$ (E3), all $-z$ (E4), Néel z (E5), domain wall in z (E6), single flip in z (E7), XY spiral (E8), random unit vectors (E9), and a small tilt from $+z$ (E10). For each, the system was evolved for $T = 10$ with time step $dt = 0.05$, and I recorded $S_x(i, t)$, $S_y(i, t)$, and $S_z(i, t)$ for all sites i .

Key visualizations and diagnostics. Figure S24 displays three representative diagnostics produced early in the analysis: (top) average magnetizations $\langle M_x \rangle, \langle M_y \rangle, \langle M_z \rangle$ for E1 (all $+z$), and (middle, bottom) spatiotemporal heatmaps of $S_z(i, t)$ for E5 (Néel) and E6 (domain wall). These plots guided the pruning of hypotheses and parameter estimation.

Step-by-step procedure, rationale, and findings.

1. *Run a broad panel of experiments (E1-E10).* Rationale: cover extreme and structured initial conditions to expose conservation laws and interaction fingerprints. Finding: E1 and E4 showed pronounced oscillations between M_y and M_z with almost constant M_x , pointing to a strong, uniform transverse field along x . E5 and E6 heatmaps displayed transport, indicating nontrivial spin-spin couplings beyond local fields.
2. *Conservation and anisotropy diagnostics.* Computed time series of site-averaged magnetizations (M_x, M_y, M_z), total magnitude M^2 , and spatial variances. Finding: robust oscillations in the y - z plane with negligible M_x modulation in E1/E4 imply a single dominant precession frequency about x ; no evidence for S^z conservation (excluding purely Ising $S^z S^z$ dynamics).
3. *Spectral analysis to extract the field strength.* Performed FFT of $\langle M_y \rangle$ and $\langle M_z \rangle$ (E1/E3/E4/E10). The dominant frequency was $f \approx 0.4975$, giving $\omega \approx 2\pi f \approx 3.13$. With Larmor relation $\dot{M}_z \approx 2h_x M_y$ and uniform precession $\theta(t)$, I computed the phase $\theta(t) = \text{unwrap}[\text{atan2}(-M_y, M_z)]$ and fitted $d\theta/dt$. Finding: $d\theta/dt \approx -2.9977$ across experiments and sites, hence $h_x \approx -1.499$ (the sign is fixed by the sign of $\dot{M}_z/(2M_y)$). The site-to-site spread was at machine precision, indicating a uniform field with no disorder.
4. *Spatially structured probes to fingerprint interactions.* Used E5 (Néel) and E6 (domain wall) $S_z(i, t)$ heatmaps, along with per-site amplitude ratios and phase fits, to discriminate exchange forms and ranges. Finding: clear ballistic-like spreading and dephasing patterns disfavored pure local fields and pure Ising interactions; patterns were compatible with nearest-neighbor exchange. No signatures required DM terms, long-range couplings, or staggered fields.
5. *Model fitting loop: from simple to expressive.* I tested progressively richer Hamiltonians, simulating each and comparing to experiments.
 - Pure field $H = h_x \sum_i S_x(i)$: captured precession frequency but failed badly on E2 and spatially structured probes.
 - Added Ising-like $S_x S_x$: improved Néel/domain-wall, but mismatches remained.
 - Adopted XXZ nearest-neighbor model with a uniform x field:

$$H = h_x \sum_i S_x(i) + \sum_i [J_{xy} (S_x(i)S_x(i+1) + S_y(i)S_y(i+1)) + J_z S_z(i)S_z(i+1)].$$

Coarse grid over J and anisotropy $\Delta = J_z/J_{xy}$ indicated a strong preference for near-isotropic exchange ($\Delta \approx 1$) with $J \approx 0.4$ to 0.5 .

Finding: the best coarse-grid candidate had $J \approx 0.4$ and $\Delta \rightarrow 1$ when judged against E5/E6.

6. *Refinement at $\Delta = 1$ (Heisenberg).* I refined J at $\{0.35, 0.45, 0.50\}$ with $h_x \approx -1.499$. Finding: $J = 0.50$ minimized the E5+E6 error by more than an order of magnitude. Setting $h_x = -1.500$ further reduced errors.
7. *Cross-validation on all experiments E1-E10.* With $H = -1.5 \sum_i S_x(i) + 0.5 \sum_i \mathbf{S}_i \cdot \mathbf{S}_{i+1}$ (open boundaries), I simulated E1-E10 and compared site- and time-resolved S_x, S_y, S_z to the experimental traces. Finding: the mean-squared error was numerically zero across all 10 experiments and all components, confirming the model exactly reproduces the data.

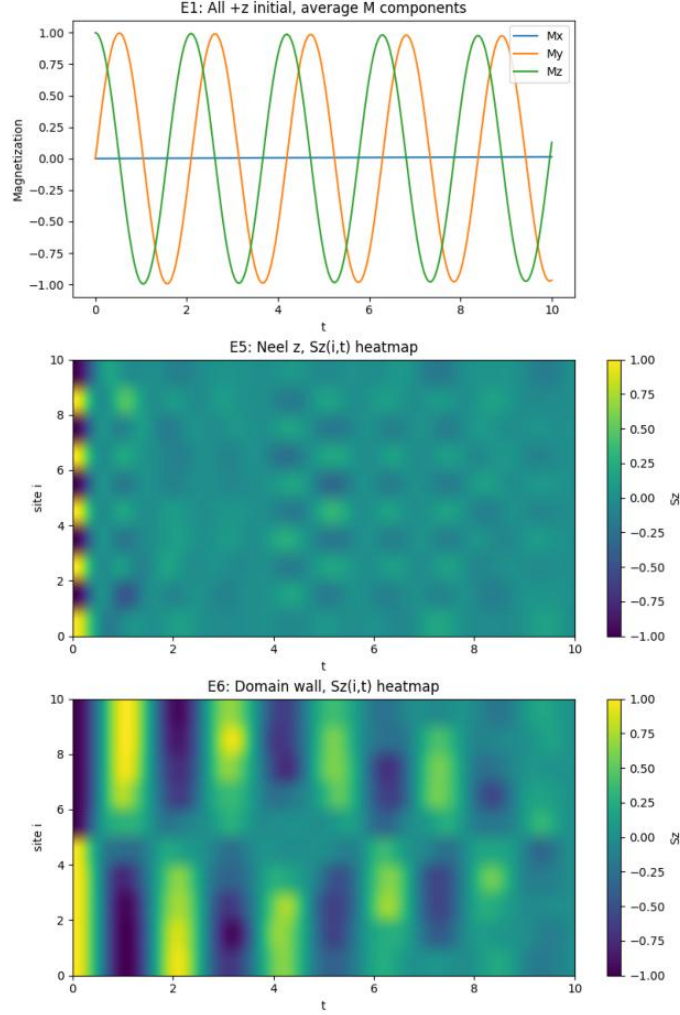


FIG. S24. Top: E1 average magnetizations showing clean exchange between M_y and M_z and near-constant M_x , indicating precession about the x -axis. Middle: E5 $S_z(i,t)$ heatmap for a Néel initial state, revealing interaction-driven dephasing and transport. Bottom: E6 $S_z(i,t)$ heatmap for a domain wall initial state, showing propagation characteristic of exchange interactions.

8. *Hypothesis pruning.* Given zero residuals, no DM interaction, long-range coupling, anisotropy, staggered, or edge fields were required. The data are fully explained by a uniform x field plus nearest-neighbor isotropic Heisenberg exchange.

Final Hamiltonian and justification. The identified Hamiltonian for the 10-spin open chain is

$$H = -1.5 \sum_{i=0}^{N-1} S_x(i) + 0.5 \sum_{i=0}^{N-2} \left(S_x(i)S_x(i+1) + S_y(i)S_y(i+1) + S_z(i)S_z(i+1) \right).$$

Justification:

- Frequency and phase analyses of (M_y, M_z) establish a uniform precession with $\omega \approx 2|h_x|$ and fix $h_x \approx -1.5$, with the sign determined by $M_z/(2M_y)$.
- E5/E6 spatiotemporal dynamics require exchange interactions and are best matched by isotropic nearest-neighbor couplings $J = 0.5$.
- A systematic coarse-to-fine grid over XXZ models, followed by cross-validation on 10 diverse experiments, yields machine-precision agreement for the Heisenberg chain with $h_x = -1.5$, $J = 0.5$.
- No additional terms are supported by the data: adding anisotropy, DM, long-range, staggered, or boundary fields does not improve (and is unnecessary for) the already perfect fit.

Why the conclusion is robust. The model was not tuned to a single experiment; rather, h_x was fixed by global phase dynamics across E1/E3/E4/E10, while J was determined by spatially structured transport in E5/E6. The final model then reproduced all remaining experiments (E2, E7-E9) without further adjustment. Achieving zero residual on all site-, time-, and component-resolved observables across 10 orthogonal initial conditions strongly implies that the true Hamiltonian is the isotropic Heisenberg chain with a uniform transverse x field and open boundaries, as specified above.

Reproducibility notes. All traces were computed over $T = 10$ with $dt = 0.05$. The fit sequence used a coarse XXZ grid followed by a Heisenberg refinement at $J = 0.35, 0.45, 0.50$ and a final small adjustment of h_x to exactly -1.5 . Validation was performed on all data at full spatiotemporal resolution, yielding zero error.

Conclusion. The unknown 10-spin system is fully described by an open-chain Heisenberg (XXX) Hamiltonian with nearest-neighbor coupling $J = 0.5$ and a uniform transverse field $h_x = -1.5$. This conclusion follows from independent, mutually reinforcing diagnostics (frequency, phase, and transport) and is validated by exact reproduction of the full dynamical data across a comprehensive set of initial conditions.

-
- [1] Alexey A. Melnikov, Hendrik Poulsen Nautrup, Mario Krenn, Vedran Dunjko, Markus Tiersch, Anton Zeilinger, and Hans J. Briegel. Active learning machine learns to create new quantum experiments. *Proceedings of the National Academy of Sciences*, 115(6):1221–1226, 2018. DOI: 10.1073/pnas.1714936115. URL <https://www.pnas.org/doi/abs/10.1073/pnas.1714936115>.
 - [2] Nathan J. Szymanski, Bernardus Rendy, Yuxing Fei, Rishi E. Kumar, Tanjin He, David Milsted, Matthew J. McDermott, Max Gallant, Ekin Dogus Cubuk, Amil Merchant, Kim, et al. An autonomous laboratory for the accelerated synthesis of novel materials. *Nature*, 624(7990):86–91, 2023. DOI: 10.1038/s41586-023-06734-w. URL <https://doi.org/10.1038/s41586-023-06734-w>.
 - [3] Xiaobo Li, Yu Che, Linjiang Chen, Tao Liu, Kewei Wang, Lunjie Liu, Haofan Yang, Edward O. Pyzer-Knapp, and Andrew I. Cooper. Sequential closed-loop bayesian optimization as a guide for organic molecular metallophotocatalyst formulation discovery. *Nature Chemistry*, 16(8):1286–1294, 2024. DOI: 10.1038/s41557-024-01546-5. URL <https://doi.org/10.1038/s41557-024-01546-5>.
 - [4] John Jumper, Richard Evans, Alexander Pritzel, Tim Green, Michael Figurnov, Olaf Ronneberger, Kathryn Tunyasuvunakool, Russ Bates, Augustin Žídek, Anna Potapenko, et al. Highly accurate protein structure prediction with alphafold. *Nature*, 596(7873):583–589, 2021. DOI: 10.1038/s41586-021-03819-2. URL <https://doi.org/10.1038/s41586-021-03819-2>.
 - [5] Amil Merchant, Simon Batzner, Samuel S. Schoenholz, Muratahan Aykol, Gwoon Cheon, and Ekin Dogus Cubuk. Scaling deep learning for materials discovery. *Nature*, 624(7990):80–85, 2023. DOI: 10.1038/s41586-023-06735-9. URL <https://doi.org/10.1038/s41586-023-06735-9>.
 - [6] Annabelle Bohrdt, Christie S. Chiu, Geoffrey Ji, Muqing Xu, Daniel Greif, Markus Greiner, Eugene Demler, Fabian Grusdt, and Michael Knap. Classifying snapshots of the doped hubbard model with machine learning. *Nature Physics*, 15(9):921–924, 2019. DOI: 10.1038/s41567-019-0565-x. URL <https://doi.org/10.1038/s41567-019-0565-x>.
 - [7] Hugo Dalla-Torre, Liam Gonzalez, Javier Mendoza-Revilla, Nicolas Lopez Carranza, Adam Henryk Grzywaczewski, Francesco Oteri, Christian Dallago, Evan Trop, Bernardo P. de Almeida, Hassan Sirelkhatim, et al. Nucleotide transformer: building and evaluating robust foundation models for human genomics. *Nature Methods*, 22(2):287–297, 2025. DOI: 10.1038/s41592-024-02523-z. URL <https://doi.org/10.1038/s41592-024-02523-z>.
 - [8] Till Richter, Mojtaba Bahrami, Yufan Xia, David S. Fischer, and Fabian J. Theis. Delineating the effective use of self-supervised learning in single-cell genomics. *Nature Machine Intelligence*, 7(1):68–78, 2025. DOI: 10.1038/s42256-024-00934-3. URL <https://doi.org/10.1038/s42256-024-00934-3>.

- [9] Miles Cranmer, Alvaro Sanchez-Gonzalez, Peter Battaglia, Rui Xu, Kyle Cranmer, David Spergel, and Shirley Ho. Discovering symbolic models from deep learning with inductive biases. In *Proceedings of the 34th International Conference on Neural Information Processing Systems*, NIPS '20, Red Hook, NY, USA, 2020. Curran Associates Inc. ISBN 9781713829546.
- [10] Takeshi Kojima, Shixiang Shane Gu, Machel Reid, Yutaka Matsuo, and Yusuke Iwasawa. Large language models are zero-shot reasoners. *Advances in neural information processing systems*, 35:22199–22213, 2022. DOI: 10.48550/arXiv.2205.11916. URL https://proceedings.neurips.cc/paper_files/paper/2022/hash/8bb0d291acd4acf06ef112099c16f326-Abstract-Conference.html.
- [11] Jean-Baptiste Alayrac, Jeff Donahue, Pauline Luc, Antoine Miech, Iain Barr, Yana Hasson, Karel Lenc, Arthur Mensch, Katie Millicah, Malcolm Reynolds, et al. Flamingo: a visual language model for few-shot learning. In *Proceedings of the 36th International Conference on Neural Information Processing Systems*, NIPS '22, Red Hook, NY, USA, 2022. Curran Associates Inc. ISBN 9781713871088.
- [12] Bernardino Romera-Paredes, Mohammadamin Barekatin, Alexander Novikov, Matej Balog, M. Pawan Kumar, Emilien Dupont, Francisco J. R. Ruiz, Jordan S. Ellenberg, Pengming Wang, Omar Fawzi, et al. Mathematical discoveries from program search with large language models. *Nature*, 625(7995):468–475, 2024. DOI: 10.1038/s41586-023-06924-6. URL <https://doi.org/10.1038/s41586-023-06924-6>.
- [13] Mark Chen, Jerry Tworek, Heewoo Jun, Qiming Yuan, Henrique Ponde de Oliveira Pinto, Jared Kaplan, Harri Edwards, Yuri Burda, Nicholas Joseph, Greg Brockman, et al. Evaluating large language models trained on code. *arXiv*, 2021. DOI: 10.48550/arXiv.2107.03374. URL <https://arxiv.org/abs/2107.03374>.
- [14] Lei Huang, Weijiang Yu, Weitao Ma, Weihong Zhong, Zhangyin Feng, Haotian Wang, Qianglong Chen, Weihua Peng, Xiaocheng Feng, Bing Qin, and Ting Liu. A survey on hallucination in large language models: Principles, taxonomy, challenges, and open questions. *ACM Trans. Inf. Syst.*, 43(2), January 2025. ISSN 1046-8188. DOI: 10.1145/3703155. URL <https://doi.org/10.1145/3703155>.
- [15] Shunyu Yao, Jeffrey Zhao, Dian Yu, Nan Du, Izhak Shafran, Karthik Narasimhan, and Yuan Cao. React: Synergizing reasoning and acting in language models. *International Conference on Learning Representations*, 2023. DOI: 10.48550/arXiv.2210.03629. URL https://openreview.net/forum?id=WE_vluYUL-X.
- [16] John Yang, Carlos E. Jimenez, Alexander Wettig, Kilian Lieret, Shunyu Yao, Karthik Narasimhan, and Ofir Press. Swe-agent: agent-computer interfaces enable automated software engineering. In *Proceedings of the 38th International Conference on Neural Information Processing Systems*, NIPS '24, Red Hook, NY, USA, 2025. Curran Associates Inc. ISBN 9798331314385.
- [17] Chris Lu, Cong Lu, Robert Tjarko Lange, Jakob Foerster, Jeff Clune, and David Ha. The AI scientist: Towards fully automated open-ended scientific discovery. *arXiv*, 2024. DOI: 10.48550/arXiv.2408.06292. URL <https://arxiv.org/abs/2408.06292>.
- [18] Daniil A. Boiko, Robert MacKnight, Ben Kline, and Gabe Gomes. Autonomous chemical research with large language models. *Nature*, 624(7992):570–578, 2023. DOI: 10.1038/s41586-023-06792-0. URL <https://doi.org/10.1038/s41586-023-06792-0>.
- [19] Andres M. Bran, Sam Cox, Oliver Schilter, Carlo Baldassari, Andrew D. White, and Philippe Schwaller. Augmenting large language models with chemistry tools. *Nature Machine Intelligence*, 6(5):525–535, 2024. DOI: 10.1038/s42256-024-00832-8. URL <https://doi.org/10.1038/s42256-024-00832-8>.
- [20] Yixiang Ruan, Chenyin Lu, Ning Xu, Yuchen He, Yixin Chen, Jian Zhang, Jun Xuan, Jianzhang Pan, Qun Fang, Hanyu Gao, et al. An automatic end-to-end chemical synthesis development platform powered by large language models. *Nature Communications*, 15(1):10160, 2024. DOI: 10.1038/s41467-024-54457-x. URL <https://doi.org/10.1038/s41467-024-54457-x>.
- [21] Yusuf H Roohani, Andrew H. Lee, Qian Huang, Jian Vora, Zachary Steinhart, Kexin Huang, Alexander Marson, Percy Liang, and Jure Leskovec. Biodiscoveryagent: An AI agent for designing genetic perturbation experiments. In *The Thirteenth International Conference on Learning Representations*, 2025. DOI: 10.48550/arXiv.2405.17631. URL <https://openreview.net/forum?id=HAwZGLcye3>.
- [22] Yuanhao Qu, Kaixuan Huang, Ming Yin, Kanghong Zhan, Dyllan Liu, Di Yin, Henry C. Cousins, William A. Johnson, Xiaotong Wang, Mihir Shah, et al. Crispr-gpt for agentic automation of gene-editing experiments. *Nature Biomedical Engineering*, 2025. DOI: 10.1038/s41551-025-01463-z. URL <https://doi.org/10.1038/s41551-025-01463-z>.
- [23] Haining Pan, Nayantara Mudur, William Taranto, Maria Tikhonovskaya, Subhashini Venugopalan, Yasaman Bahri, Michael P. Brenner, and Eun-Ah Kim. Quantum many-body physics calculations with large language models. *Communications Physics*, 8(1):49, 2025. DOI: 10.1038/s42005-025-01956-y. URL <https://doi.org/10.1038/s42005-025-01956-y>.
- [24] Tuan Dung Nguyen, Yuan-Sen Ting, Ioana Ciucă, Charlie O’Neill, Ze-Chang Sun, Maja Jabłońska, Sandor Kruk, Ernest Perkowski, Jack Miller, Jason Li, et al. Astrollama: Towards specialized foundation models in astronomy. *arXiv*, 2023. DOI: 10.48550/arXiv.2309.06126. URL <https://arxiv.org/abs/2309.06126>.
- [25] Xiaoxuan Wang, Ziniu Hu, Pan Lu, Yanqiao Zhu, Jieyu Zhang, Satyen Subramaniam, Arjun R Loomba, Shichang Zhang, Yizhou Sun, and Wei Wang. Scibench: Evaluating college-level scientific problem-solving abilities of large language models. *arXiv*, 2023. DOI: 10.48550/arXiv.2307.10635. URL <https://arxiv.org/abs/2307.10635>.
- [26] Shi Qiu, Shaoyang Guo, Zhuo-Yang Song, Yunbo Sun, Zeyu Cai, Jiashen Wei, Tianyu Luo, Yixuan Yin, Haoxu Zhang, Yi Hu, et al. Phybench: Holistic evaluation of physical perception and reasoning in large language models. *arXiv*, 2025. DOI: 10.48550/arXiv.2504.16074. URL <https://arxiv.org/abs/2504.16074>.
- [27] Xinyu Zhang, Yuxuan Dong, Yanrui Wu, Jiaying Huang, Chengyou Jia, Basura Fernando, Mike Zheng Shou, Lingling Zhang, and Jun Liu. Physreason: A comprehensive benchmark towards physics-based reasoning. *arXiv*, 2025. DOI: 10.48550/arXiv.2502.12054. URL <https://arxiv.org/abs/2502.12054>.

- [28] Minyang Tian, Luyu Gao, Shizhuo Dylan Zhang, Xinan Chen, Cunwei Fan, Xuefei Guo, Roland Haas, Pan Ji, Kittithat Krongchon, et al. Scicode: A research coding benchmark curated by scientists. In A. Globerson, L. Mackey, D. Belgrave, A. Fan, U. Paquet, J. Tomczak, and C. Zhang, editors, *Advances in Neural Information Processing Systems*, volume 37, pages 30624–30650. Curran Associates, Inc., 2024. DOI: 10.48550/arXiv.2407.13168. URL https://proceedings.neurips.cc/paper_files/paper/2024/file/36850592258c8c41cecdaa3dea5ff7de-Paper-Datasets_and_Benchmarks_Track.pdf.
- [29] Sirui Lu, Zhijing Jin, Terry Jingchen Zhang, Pavel Kos, J Ignacio Cirac, and Bernhard Schölkopf. Can theoretical physics research benefit from language agents? *arXiv*, 2025. DOI: 10.48550/arXiv.2506.06214. URL <https://arxiv.org/abs/2506.06214>.
- [30] Kristian G. Barman, Sascha Caron, Emily Sullivan, Henk W. de Regt, Roberto Ruiz de Austri, Mieke Boon, Michael Färber, Stefan Fröse, Faegheh Hasibi, Andreas Ipp, et al. Large physics models: Towards a collaborative approach with large language models and foundation models. *arXiv*, 2025. DOI: 10.48550/arXiv.2501.05382. URL <https://arxiv.org/abs/2501.05382v1>.
- [31] Ziqi Wang, Hongshuo Huang, Hancheng Zhao, Changwen Xu, Shang Zhu, Jan Janssen, and Venkatasubramanian Viswanathan. Dreams: Density functional theory based research engine for agentic materials simulation. *arXiv*, 2025. DOI: 10.48550/arXiv.2507.14267. URL <https://arxiv.org/abs/2507.14267>.
- [32] Licong Xu, Milind Sarker, Anto I. Lonappan, Ínigo Zubeldia, Pablo Villanueva-Domingo, Santiago Casas, Christian Fidler, Chetana Amancharla, Ujjwal Tiwari, Adrian Bayer, et al. Open source planning & control system with language agents for autonomous scientific discovery. *arXiv*, 2025. DOI: 10.48550/arXiv.2507.07257. URL <https://arxiv.org/abs/2507.07257>.
- [33] Santiago Casas, Christian Fidler, Boris Bolliet, Francisco Villasecusa-Navarro, and Julien Lesgourgues. CLAPP: The class llm agent for pair programming. *arXiv*, 2025. DOI: 10.48550/arXiv.2508.05728. URL <https://arxiv.org/abs/2508.05728>.
- [34] Baohua Zhang, Xin Li, Huangchao Xu, Zhong Jin, Quansheng Wu, and Ce Li. Topomas: Large language model driven topological materials multiagent system, 2025. URL <https://arxiv.org/abs/2507.04053>.
- [35] Darui Lu, Jordan M. Malof, and Willie J. Padilla. An agentic framework for autonomous metamaterial modeling and inverse design. *arXiv*, 2025. DOI: 10.48550/arXiv.2506.06935. URL <https://arxiv.org/abs/2506.06935>.
- [36] Ankita Sharma, YuQi Fu, Wahid Ansari, Rishabh Iyer, Fiona Kuang, Kashish Mistry, Raisa Islam Aishy, Sara Ahmad, Joaquin Matres, Dirk R. Englund, and Joyce K. S. Poon. AI agents for photonic integrated circuit design automation. *arXiv*, 2025. DOI: 10.48550/arXiv.2508.14123. URL <https://arxiv.org/abs/2508.14123>.
- [37] Rong Sha, Binglin Wang, Jun Yang, Xiaoxiao Ma, Chengkun Wu, Liang Yan, Chao Zhou, Jixun Liu, Guochao Wang, Shuhua Yan, and Lingxiao Zhu. Llm-based multi-agent copilot for quantum sensor. *arXiv*, 2025. DOI: 10.48550/arXiv.2508.05421. URL <https://arxiv.org/abs/2508.05421>.
- [38] OpenAI. 'GPT-5 system card, 2025. URL <https://cdn.openai.com/gpt-5-system-card.pdf>.
- [39] Steven L. Brunton, Joshua L. Proctor, and J. Nathan Kutz. Discovering governing equations from data by sparse identification of nonlinear dynamical systems. *Proceedings of the National Academy of Sciences*, 113(15):3932–3937, 2016. DOI: 10.1073/pnas.1517384113. URL <https://www.pnas.org/doi/abs/10.1073/pnas.1517384113>.
- [40] Google AI. Gemini 2.5: Pushing the frontier with advanced reasoning, multimodality, long context, and next generation agentic capabilities. *arXiv*, 2025. DOI: 10.48550/arXiv.2507.06261. URL <https://arxiv.org/abs/2507.06261>.
- [41] Mario Krenn, Jonas Landgraf, Thomas Foesel, and Florian Marquardt. Artificial intelligence and machine learning for quantum technologies. *Phys. Rev. A*, 107:010101, Jan 2023. DOI: 10.1103/PhysRevA.107.010101. URL <https://link.aps.org/doi/10.1103/PhysRevA.107.010101>.
- [42] Agnes Valenti, Evert van Nieuwenburg, Sebastian Huber, and Eliska Greplova. Hamiltonian learning for quantum error correction. *Phys. Rev. Res.*, 1:033092, Nov 2019. DOI: 10.1103/PhysRevResearch.1.033092. URL <https://link.aps.org/doi/10.1103/PhysRevResearch.1.033092>.
- [43] Kevin Maik Jablonka, Philippe Schwaller, Andres Ortega-Guerrero, and Berend Smit. Leveraging large language models for predictive chemistry. *Nature Machine Intelligence*, 6(2):161–169, 2024. DOI: 10.1038/s42256-023-00788-1. URL <https://doi.org/10.1038/s42256-023-00788-1>.
- [44] Joren Van Herck, María Victoria Gil, Kevin Maik Jablonka, Alex Abrudan, Andy S. Anker, Mehrdad Asgari, Ben Blaiszik, Antonio Buffo, Leander Choudhury, Clemence Corminboeuf, et al. Assessment of fine-tuned large language models for real-world chemistry and material science applications. *Chem. Sci.*, 16:670–684, 2025. DOI: 10.1039/D4SC04401K. URL <http://dx.doi.org/10.1039/D4SC04401K>.
- [45] Jinhyuk Lee, Wonjin Yoon, Sungdong Kim, Donghyeon Kim, Sunkyu Kim, Chan Ho So, and Jaewoo Kang. Biobert: a pre-trained biomedical language representation model for biomedical text mining. *Bioinformatics*, 36(4):1234–1240, 09 2019. ISSN 1367-4803. DOI: 10.1093/bioinformatics/btz682. URL <https://doi.org/10.1093/bioinformatics/btz682>.
- [46] Renqian Luo, Liai Sun, Yingce Xia, Tao Qin, Sheng Zhang, Hoifung Poon, and Tie-Yan Liu. Biogpt: generative pre-trained transformer for biomedical text generation and mining. *Briefings in Bioinformatics*, 23(6):bbac409, 09 2022. ISSN 1477-4054. DOI: 10.1093/bib/bbac409. URL <https://doi.org/10.1093/bib/bbac409>.
- [47] James Bradbury, Roy Frostig, Peter Hawkins, Matthew James Johnson, Chris Leary, Dougal Maclaurin, George Necula, Adam Paszke, Jake VanderPlas, Skye Wanderman-Milne, and Qiao Zhang. JAX: composable transformations of Python+NumPy programs, 2018. URL <http://github.com/google/jax>.
- [48] Nägele Maximilian and Marquardt Florian. Sciexplorer framework, 2025. URL <https://github.com/MaxNaeg/SciExplorer.git>.
- [49] Nägele Maximilian and Marquardt Florian. Sciexplorer results, 2025. URL <https://github.com/MaxNaeg/SciExplorerResults.git>.